Research Square

Preprints are preliminary reports that have not undergone peer review.
They should not be considered conclusive, used to inform clinical practice,
or referenced by the media as validated information.

Satellite attribution of trace gases to gas flares in the Niger Delta, Nigeria, 2012–2024: a transport-corrected framework with null tests

Progress Peter Akpan

progresspeter2@gmail.com

Sambus Geospatial Nigeria Limited

Research Article

Keywords: Gas flaring, TROPOMI, VIIRS Nightfire, source attribution, placebo test, Niger Delta, carbon monoxide, methane

Posted Date: November 20th, 2026

DOI: https://doi.org/10.21203/rs.3.rs-11798156/v1

License: This work is licensed under a Creative Commons Attribution 4.0 International License.
Read Full License

Additional Declarations: No competing interests reported.

Satellite attribution of trace gases to gas flares in the Niger Delta, Nigeria, 2012–2024: a transport-corrected framework with null tests

Progress Peter Akpan

Sambus Geospatial Nigeria Limited, Lagos, Nigeria

Corresponding author: Progress Peter Akpan (progresspeter2@gmail.com)

Highlights

- Niger Delta flared gas fell 32% from 2012 to 2024 as onshore flare numbers rose
- Satellite-observed flaring ran 13–20% above operator-reported volumes in 2023–2024
- Placebo-adjusted CO excess of 78 µmol/m² at onshore flares, largest within 2 km
- Null tests corrected a threefold overstatement in wind-rotated CO attribution
- Methane over the flaring zone exceeded the regional background by 5.3 ppb

Keywords

Gas flaring; TROPOMI; VIIRS Nightfire; source attribution; placebo test; Niger Delta; carbon monoxide; methane

Abstract

Gas flaring in Nigeria's Niger Delta wastes gas and degrades air quality, yet satellite estimates of its emissions are rarely tested for bias. This study combines VIIRS Nightfire flare detections, Sentinel-5P TROPOMI CO, SO_2 and CH_4, and ERA5 winds at the satellite overpass hour in a transport-corrected multi-sensor attribution framework (TCMSAF) with built-in null tests: flare-free placebo points, crosswind controls and fixed compass sectors that cancel static geography. Flared gas in the nine Niger Delta states fell 32% from 2012 to 2024 (9.69 to 6.58 BCM; Theil–Sen −0.29 BCM/yr, $p < 0.001$), steepest offshore (−46% against −20% onshore), while active onshore flares increased from 103 to 133. Satellite-observed volumes agreed with operator reports to within 6% over 2021–2024 but ran 13–20% higher in 2023–2024 as new onshore flares appeared, a gap worth about US$79 million in flare penalties in 2024. With fixed sectors and placebo adjustment, onshore flare sites carried a CO excess of 78 µmol/m² (95% CI 14 to 142) that was largest within 2 km of flares and decreased with distance, the opposite of what a background gradient produces; it was strongest in the Harmattan season and on light-wind days. Bias-corrected XCH_4 over the flaring zone exceeded a latitude-adjusted background by 5.3 ppb (95% CI 2.4 to 8.1). The null tests also showed that the conventional wind-rotated contrast (241 µmol/m²) overstated the flare CO signal about threefold, because placebo points (−151 µmol/m²) and crosswind sectors (+120 µmol/m²) revealed regional structure of the same size. Flare-attributable SO_2 and offshore CO were below detection at TROPOMI resolution. The framework runs on public data in Google Earth Engine and gives regulators an independent, reproducible check on reported flaring and its air-quality footprint.

1 Introduction

Gas flaring in the Niger Delta has burned associated gas from oil production for more than six decades, and Nigeria remains one of the nine countries that together accounted for 83% of global gas flaring in 2025 (World Bank, 2026). Flares emit carbon monoxide (CO), sulphur dioxide (SO_2), black carbon and

unburned methane (CH_4), and their pollution reaches the dense settlements that surround many flow stations (Anejionu et al., 2015a; Fawole et al., 2016). Flares are also a climate concern: inefficient and unlit flares release far more methane than the 98% destruction efficiency usually assumed (Plant et al., 2022), and oil and gas facilities include some of the largest methane point sources seen from space (Lauvaux et al., 2022).

Satellites now observe both the flares and the gases. VIIRS Nightfire detects combustion sources at night and estimates flared volumes for each flare worldwide (Elvidge et al., 2013, 2016), and earlier sensors were used to map flares and their volumes in the Niger Delta (Anejionu et al., 2015b). Since 2018, the TROPOMI instrument on Sentinel-5 Precursor has mapped CO, SO_2 and CH_4 columns daily at 5.5 × 7 km (Veefkind et al., 2012; Landgraf et al., 2016; Theys et al., 2017; Lorente et al., 2021). Together these make it possible, in principle, to link each flare to the gases around it.

The usual way to make that link is to compare concentrations downwind of a source with a background, often the upwind side, after rotating the sampling geometry with the wind. Wind-resolved methods of this kind have estimated emissions from megacities and large point sources (Beirle et al., 2011; Fioletov et al., 2015, 2016), and plume inversions now quantify single methane sources (Varon et al., 2018). Their key assumption is that, apart from the source, the downwind and background areas are alike. For large, isolated sources this holds well enough. For the Niger Delta's hundreds of small flares, set among a coast-to-inland gradient, a land–sea boundary, wetlands, settlements and other combustion sources, it may not.

When it fails, a downwind excess can be produced by geography rather than by the flare, and nothing in a standard analysis reveals it. Fields that rely on observational contrasts guard against this with falsification tests: the same analysis run where the effect cannot exist, which should return zero. Such tests are rarely reported in satellite source attribution.

1.1 Satellite detection and quantification of gas flaring

Flares are among the hottest persistent surface features on Earth, and they have been mapped from orbit for three decades. The first global inventories used the low-light imaging of the DMSP Operational Linescan System, which records flares as stable night-time lights, and calibrated the summed brightness of each country against reported volumes (Elvidge et al., 2009). Night-time lights saturate over large flares and cannot separate flares from towns, so later work turned to short-wave and mid-wave infrared sensors that see the combustion itself. Along-track scanning radiometers (ATSR-2, AATSR) were used to detect flares as hot night-time anomalies at 1.6 and 3.7 µm (Casadio et al., 2012), and the series was extended to Sentinel-3 SLSTR, giving global flare inventories that now span more than 25 years (Caseiro et al., 2020; Fisher and Wooster, 2019).

The Visible Infrared Imaging Radiometer Suite (VIIRS) on Suomi-NPP and NOAA-20 changed the field. Its night-time short-wave infrared bands, collected at 750 m resolution across a 3,000 km swath, are not saturated by flares, and the Nightfire algorithm fits a Planck curve to each hot pixel to retrieve temperature, source area and radiant heat (Elvidge et al., 2013). Flares are separated from biomass fires and industrial sources by their temperature (typically 1,500–2,000 K) and their persistence, and the annual sum of radiant heat at each site is converted to a gas volume using a calibration against country-reported volumes (Elvidge et al., 2016). This is the basis of the World Bank Global Gas Flaring Reduction

Partnership estimates, which put global flaring at roughly 140 BCM a year over the past decade, and of the annual site-level files used in this study.

The volumes are model estimates, not measurements. The calibration assumes a single relation between radiant heat and gas volume for every flare, whatever its design, gas composition or combustion efficiency. Zhizhin et al. (2021) compared VIIRS estimates for Russia with operator data and found that the method underestimates the largest flares and overestimates small, persistent ones, partly because large flares are often obscured by cloud or smoke and partly because detection frequency, not only intensity, drives the annual total. Brandt (2020) compared VIIRS-derived volumes with reported offshore volumes in nine countries and found that agreement varied widely between countries and installations. Reviews of the satellite record conclude that detection is mature but conversion to volume, and especially to emissions, remains the weak link (Faruolo et al., 2021). Elvidge et al. (2018) nonetheless used the VIIRS record to quantify how much flaring reductions could contribute to national greenhouse-gas targets, because it is the only consistent global reference; national reporting is incomplete and uses differing definitions.

Volume is also not the quantity that matters for air quality or climate. What a flare emits depends on how completely it burns. Field measurements in the Bakken found combustion efficiencies above 98% for most flares but much lower values for a minority (Gvakharia et al., 2017), and aircraft surveys in the Permian found that unlit and inefficient flares release far more methane than inventories assume (Plant et al., 2022). Flare emission factors for black carbon, CO and methane are therefore uncertain by large factors (Böttcher et al., 2021; Fawole et al., 2016), and flaring has been identified as a major source of black carbon in the Arctic (Stohl et al., 2013). This gap, between a well-observed volume and a poorly constrained emission, is the reason to look for flare signals in the trace-gas record directly.

1.2 Flaring in the Niger Delta: volumes, reporting and regulation

Nigeria has flared associated gas since commercial oil production began at Oloibiri in 1958, and it has consistently ranked among the ten largest flaring countries in the World Bank series. Most of the gas is flared at flow stations and offshore platforms where associated gas has no route to market, in a region where pipeline vandalism, crude theft and insecurity have repeatedly disrupted gas-gathering projects. Successive policies have set deadlines to end routine flaring: the Associated Gas Re-injection Act of 1979, the Flare Gas (Prevention of Waste and Pollution) Regulations of 2018, which raised penalties to US$2.00 per thousand standard cubic feet for large producers, the Nigerian Gas Flare Commercialisation Programme, and the Petroleum Industry Act of 2021. Nigeria has endorsed the World Bank Zero Routine Flaring by 2030 initiative. Each earlier deadline was missed.

Remote sensing has been used to track Nigerian flaring for two decades. Anejionu et al. (2015b) used MODIS imagery to detect Niger Delta flares and estimate volumes at individual flow stations, showing that most flaring is concentrated in Rivers, Delta, Bayelsa and Akwa Ibom and that many flares are close to settlements. Anejionu et al. (2015a) described the Delta as a global air-pollution hotspot and traced the spatial and temporal variation of flaring's contribution to it. National monitoring now relies on the Nigerian Gas Flare Tracker, operated by the National Oil Spill Detection and Response Agency (NOSDRA), which converts VIIRS detections into flare-by-flare volumes. Ndunagu et al. (2021) compared the tracker with monthly volumes reported by operators to NNPC for seven offshore fields and found moderately

strong correlation (r = 0.31–0.64) but significant biases in both directions at individual fields, recommending a hybrid of the two.

The consequences for the people of the Delta have been documented in health, environmental and social studies. Flares heat the ground around them, deposit soot, and acidify rain, and residents attribute respiratory illness and crop damage to them. Fawole et al. (2016) reviewed the black-carbon and gaseous emissions from flaring and highlighted that emission factors for West African flares are essentially unmeasured. The DACCIWA campaign showed that southern West Africa has a complex, polluted atmosphere in which emissions from cities, biomass burning and the oil industry overlap under persistent monsoon flow (Knippertz et al., 2015). Against this background, whether flares produce a separable signal in satellite trace-gas columns is not obvious: the region is one of the most polluted and cloudiest on the continent, and flares are mixed with every other source of combustion.

1.3 Detecting point-source emissions in satellite trace-gas columns

Satellite detection of individual emission sources began with NO_2 and SO_2, whose short lifetimes keep plumes close to their source. Beirle et al. (2011) showed that the NO_2 column downwind of a megacity, sorted by wind direction, decays at a rate that yields both the lifetime and the emission, and the same idea, rotating each observation into a wind-aligned frame, has since become the standard way to estimate point-source emissions. Fioletov et al. (2015, 2016) fitted plume models to OMI SO_2 around more than 500 sources, building a global catalogue of point-source SO_2 emissions that has been extended to TROPOMI (Fioletov et al., 2020). Beirle et al. (2019) used the divergence of the TROPOMI NO_2 flux to map NO_x sources at the scale of individual power plants, and Goldberg et al. (2019) estimated city and power-plant NO_x emissions from TROPOMI with wind-rotated averages.

The TROPOspheric Monitoring Instrument (TROPOMI), launched on Sentinel-5P in 2017, provides daily global coverage at 5.5 × 3.5 km (7 × 7 km before August 2019) with an overpass near 13:30 local time (Veefkind et al., 2012). Its CO product, retrieved from the 2.3 µm band with the SICOR algorithm, is sensitive to the whole column including the boundary layer (Landgraf et al., 2016), and individual fire and city plumes are visible in single overpasses (Borsdorff et al., 2018). Its SO_2 product resolves volcanic and industrial plumes but has a noise level well above typical flare emissions (Theys et al., 2017). Its methane product is the most demanding: XCH_4 retrievals need clear sky and a bright, uniform surface, and are corrected for albedo-dependent biases (Lorente et al., 2021; Schneising et al., 2019).

For methane, TROPOMI has detected oil and gas basins (de Gouw et al., 2020; Schneising et al., 2020), individual blowouts and super-emitters (Lauvaux et al., 2022), and anomalously large point sources at oil and gas facilities when combined with high-resolution imagers (Varon et al., 2019). Mass-balance methods convert single methane plumes into emission rates (Varon et al., 2018). These successes share a property that Niger Delta flares lack: the sources are either very large, isolated in clean air, or seen against a uniform background. A flare burning 0.03 BCM a year with high combustion efficiency emits a small fraction of the CO of a large city, and the Delta's cloud cover removes most methane retrievals altogether.

1.4 Attribution, confounding and falsification tests

Wind rotation rests on an assumption that is rarely tested: that the only systematic difference between the downwind and upwind sides of a source is the source itself. That holds when the wind direction is

random with respect to the background. It fails when the wind is persistent and the background has a spatial gradient, because the downwind side then samples one part of the gradient on most days. In a monsoon climate such as the Gulf of Guinea, where south-westerly flow prevails for most of the year and pollution rises from the ocean inland, every point along the coast will show an apparent downwind excess. The problem is a form of confounding familiar from observational statistics: the treatment (being downwind) is correlated with an unobserved covariate (position on the gradient).

Observational sciences have developed tools to detect such confounding. Placebo, or falsification, tests apply the same estimator where no effect should exist and ask whether it returns zero; in comparative case studies these are the basis of inference for synthetic control methods (Abadie et al., 2010). Negative-control outcomes and directions, analogous here to crosswind sectors, test whether the estimator responds to things it should not. When observations are clustered, as days are within flares, standard errors must be computed at the cluster level, and with few or unbalanced clusters a bootstrap over clusters is preferred (Cameron et al., 2008; Efron, 1979). Trends in short environmental series are commonly tested with robust nonparametric statistics, the Theil–Sen slope and the Mann–Kendall test (Mann, 1945; Sen, 1968).

These tools are rarely used in satellite source attribution. Most studies validate a detection by its plausibility, its shape, or its agreement with an inventory, not by asking whether the same method would also find a signal where there is no source. Where that question has been asked, for example by sampling background regions in TROPOMI methane studies, it has shown that retrieval artefacts and surface features can produce apparent enhancements. A framework that makes falsification a required step, rather than an afterthought, is missing.

1.5 Research gap and objectives

Three gaps follow. First, satellite flare volumes for Nigeria have been compared with reported volumes only for a few offshore fields, not for the region as a whole over the full VIIRS record. Second, no study has asked whether Niger Delta flares leave a detectable signal in TROPOMI CO, SO_2 and methane, or how large that signal is once confounders are removed. Third, wind-rotated attribution has not been subjected to systematic falsification in a monsoon setting where it is most likely to fail.

This study builds them in. We present TCMSAF, a transport-corrected multi-sensor source attribution framework that combines VIIRS Nightfire, TROPOMI and ERA5 winds at the satellite overpass hour, and adds a falsification layer of placebo points, crosswind controls and a fixed-sector design that cancels static geography. Applied to the Niger Delta, we (i) quantify flaring trends from 2012 to 2024; (ii) estimate flare-attributable CO and SO_2 for 2019–2024 with and without the null tests; and (iii) assess the regional methane enhancement over the flaring zone. The main contribution is methodological. The null tests reduce the apparent CO signal at onshore flares about threefold, and we argue that they should accompany any sector-based attribution in heterogeneous regions.

2 Study area and data

2.1 Study area

The study covers the nine oil-producing states of the Niger Delta: Abia, Akwa Ibom, Bayelsa, Cross River, Delta, Edo, Imo, Ondo and Rivers, with their offshore waters in the Gulf of Guinea (Figure 1). The region

is low-lying, with mangrove and freshwater swamp forest near the coast, farmland and forest inland, and fast-growing settlements around Port Harcourt, Warri and other oil towns. South-westerly monsoon winds prevail for most of the year; the north-easterly Harmattan brings dry, dusty air from December to February.

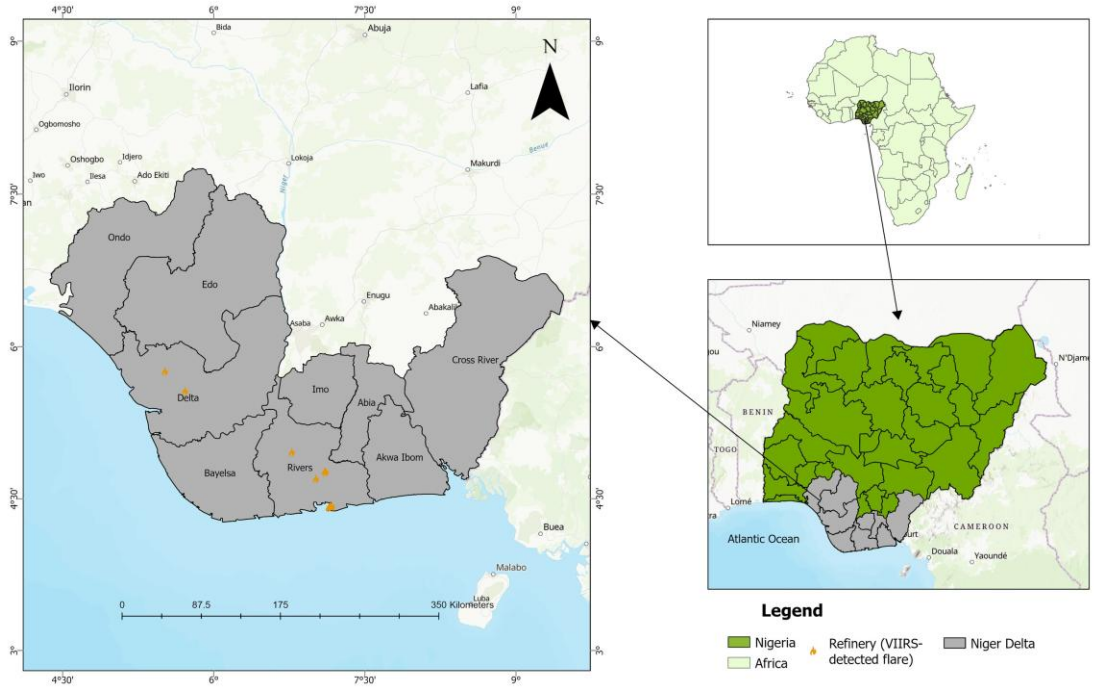

Figure 1. Study area. Main map: the nine Niger Delta states (grey) and the ten refinery, LNG and gas-processing sites with VIIRS-detected flares (flame symbols). Insets: Nigeria within Africa (top) and the Niger Delta within Nigeria (bottom). Small modular refineries, which have no VIIRS-detected flares, are not shown. Basemap: Esri World Topographic Map.

2.2 Data

All satellite and reanalysis data were processed in Google Earth Engine (Gorelick et al., 2017). Table 1 lists the datasets.

Dataset	Variable	Resolution	Period	Use	Reference
VIIRS Nightfire (EOG)	Flare location and annual flared volume (BCM)	~750 m, annual	2012–2024	Flare panel, trends	Elvidge et al. (2013, 2016)
Sentinel-5P TROPOMI L3 OFFL	CO column (mol/m²)	0.01° grid, daily	2019–2024	Flare attribution	Landgraf et al. (2016)
Sentinel-5P TROPOMI L3	SO_2 column (mol/m²)	0.01° grid, daily	2019–2024	Flare attribution	Theys et al. (2017)

Dataset	Variable	Resolution	Period	Use	Reference
OFFL					
Sentinel-5P TROPOMI L3 OFFL	Bias-corrected XCH_4 (ppb)	0.01° grid, daily	2019–2024	Regional methane	Lorente et al. (2021)
ERA5 hourly	100 m and 10 m wind	0.25°, hourly	2019–2024	Plume direction	Hersbach et al. (2020)
Hansen Global Forest Change v1.13	Land/water mask	30 m	static	Land–sea checks	Hansen et al. (2013)
SRTM	Elevation	30 m	static	Placebo and background masks	Farr et al. (2007)
ESA WorldCover v200	Wetland, mangrove, water fraction	10 m	2021	Methane regression	Zanaga et al. (2022)
FAO GAUL 2015	State boundaries	vector	static	State and onshore/offshore assignment	FAO (2015)

Table 1. Datasets.

The flare panel was built from the World Bank and Earth Observation Group VIIRS flaring files for 2012–2024, whose column names and site identifiers change between years. Records were harmonised to one row per flare per year; zero-volume rows and a duplicated 2019 LNG record were removed, and detections within 1 km of each other in different years were treated as the same flare, giving each a persistent identifier. Each flare was assigned to the nearest state in FAO GAUL level 1 and classed onshore if it lay within 1 km of a state polygon, otherwise offshore. The panel holds 2,192 flare-years in the nine states, of which 1,019 fall in the TROPOMI period, 2019–2024.

TROPOMI Level-3 products were taken from the Earth Engine catalogue (COPERNICUS/S5P/OFFL), which grids the operational Level-2 retrievals to 0.01° and keeps pixels above each product's quality threshold. The CO retrieval uses shortwave-infrared radiances (Landgraf et al., 2016; Borsdorff et al., 2018) and SO_2 the ultraviolet (Theys et al., 2017). For methane we used the bias-corrected XCH_4 column, which removes the retrieval's dependence on surface albedo (Lorente et al., 2021).

3 Methods

3.1 Framework overview

TCMSAF has three stages (Figure 2). VIIRS Nightfire supplies flare locations and volumes. For every flare and day, TROPOMI columns are sampled in sectors around the flare, with the plume direction taken from ERA5 at the overpass hour. The falsification layer then asks whether the resulting contrast is specific to flares, using placebo points, crosswind sectors and fixed compass sectors. Only an estimate that survives these tests is reported as flare-attributable.

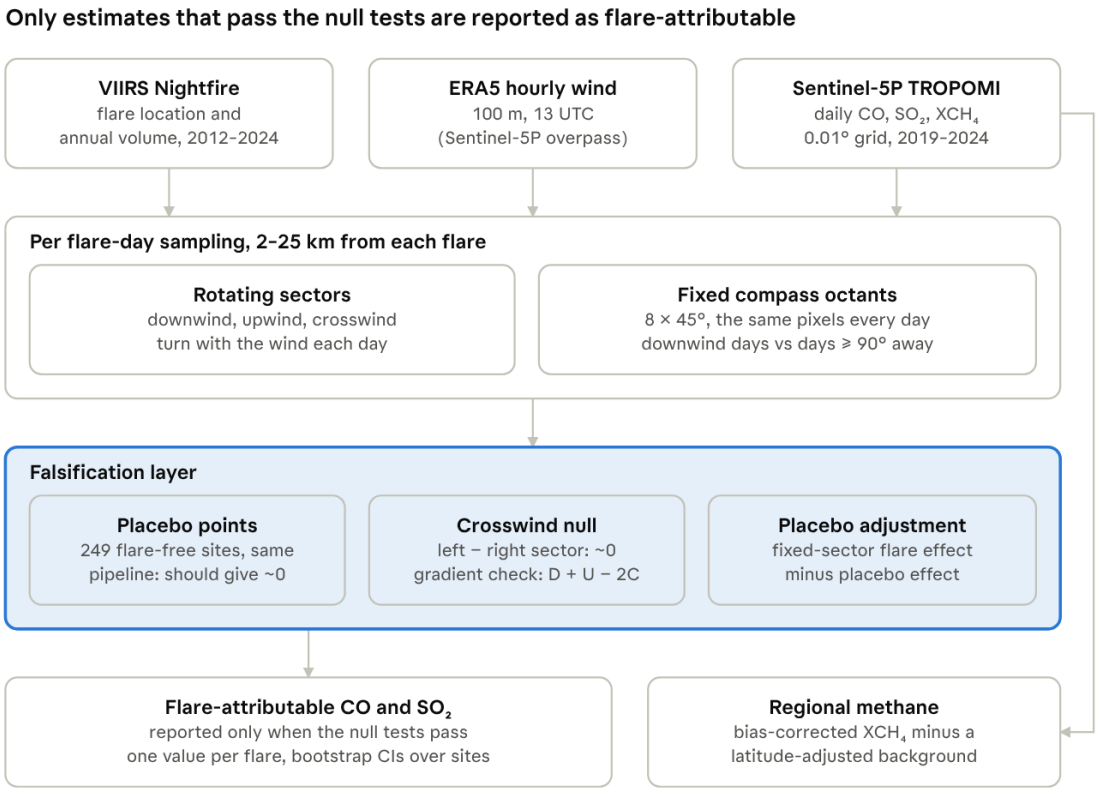

TCMSAF workflow · 3 inputs, 2 sampling designs, 3 null tests, 2 outputs

Figure 2. The TCMSAF workflow. Methane takes a separate regional route because TROPOMI XCH_4 is too sparse for flare-by-flare sampling.

3.2 Flaring trends

Annual flared volume and active flare counts were summed by state, by onshore and offshore, and for the whole region for 2012–2024. Trends were estimated with the Theil–Sen slope (Sen, 1968) and tested with the Mann–Kendall test (Mann, 1945). Flare turnover was measured as the number of flares active in a year that were not active the year before.

3.3 Per-overpass sampling and wind

Plume direction for each flare-day was taken from ERA5 hourly 100 m winds at 13:00 UTC. Sentinel-5P has an ascending-node local solar time of 13:30, which at the Niger Delta's mean longitude (~6° E) corresponds to about 13:05 UTC. Wind direction was converted to the bearing toward which air moves, and the 100 m level was used because flare plumes are released from stacks and rise buoyantly above the surface layer.

Around each flare, daily TROPOMI means were extracted in a downwind sector and an upwind sector, each 45° wide and 2–25 km from the flare, plus downwind distance bands at 0–2, 2–5, 5–10 and 10–20 km. Because TROPOMI's wide swath samples off-nadir pixels over the Delta between roughly 12:15 and 13:55 UTC, all 2023 results were recomputed with winds at 12, 13 and 14 UTC (Table S1).

Figure 3 draws both sampling designs around one onshore flare in Rivers State (site NDF0104). The rotating sectors turn with the ERA5 wind each day, so the same ground can be downwind on one day and upwind on the next. The fixed octants never move on each day the octant the wind blows into is compared with the background octants, leaving out the two octants next to it, which can catch the edge of the plume.

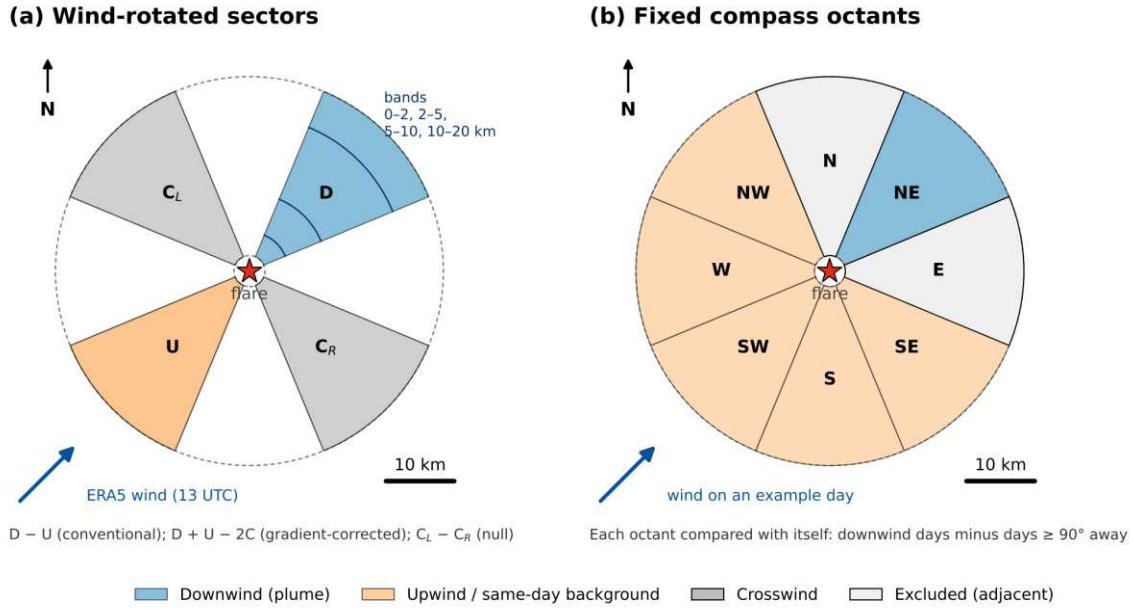

Figure 3. Sampling designs around an example onshore flare (NDF0104, Rivers State). (a) Rotating sectors: downwind (D), upwind (U) and two crosswind (C) sectors, each 45° wide, turned every day to the ERA5 13 UTC wind (arrow); rings mark the 2, 5, 10 and 20 km distance bands used for the distance-decay analysis. (b) Fixed compass octants: on a day with transport toward the north-east, the NE octant is downwind (blue), the two adjacent octants are excluded (grey) and the remaining five form the background (orange).

3.4 Statistical unit and inference

A flare-day was usable when the 100 m wind speed was at least 2 m/s and each sector compared held at least three valid TROPOMI pixels. For each flare-year with at least five usable days, the daily contrasts were averaged, and a one-sided Wilcoxon signed-rank test was applied as a descriptive flag.

The same flare appears in up to six years, so flare-years are not independent. Pooled means and the share of flare-years flagged significant therefore carry 95% confidence intervals from a cluster bootstrap (2,000 resamples of whole sites). Comparisons between flares and placebo points use a one-sided Mann–Whitney test on one value per site, its mean over years. Daily contrasts are autocorrelated, so the Wilcoxon flag is judged against its empirical rate at placebo points, not against a nominal 5%.

3.5 Null tests

Placebo points. The identical processing (same ERA5 hour, sector geometry, pixel and wind rules, and statistics) was applied to 249 placebo points for 2019–2024. Candidates were drawn at random inside Nigeria within 3.8–10° E and 4–8° N. They were kept if they lay below 300 m elevation, at least 50 km from any flare detected in 2012–2024, and at least 40 km from central Lagos. Because the 50 km exclusion pushes candidates north of the Delta, points were stratified in 0.25° latitude bins in proportion to the onshore flares, with short bins topped up by the candidates nearest the flares' median latitude. A method free of geographic artefacts should give a placebo contrast near zero.

Crosswind control. Two further sectors were extracted each day, centred 90° left (L) and right (R) of the plume heading, with the same ring and width. With no spatial structure, L − R should be near zero.

Gradient-corrected estimator. If the background varies linearly in space in any direction, the downwind (D), upwind (U) and mean crosswind (C) sectors satisfy D = a + g + F, U = a − g and C = a, where F is the flare contribution. The combination

```
\Delta_{\mathrm{grad}} = D + U - 2C
```

cancels the gradient and leaves F. Plume reaching the crosswind sectors would raise C and bias this estimate low, so it is a lower bound. A within-flare test also regressed each flare's yearly contrast on its yearly volume, with site and year fixed effects and standard errors clustered by site.

3.6 Fixed-sector design

Flare-attributable CO and SO_2 were estimated with sectors that stay fixed in space, so that each part of the landscape is compared only with itself. Around each flare and placebo point, daily TROPOMI means were extracted in eight compass octants (centred on N, NE, …, NW; 45° wide, 2–25 km). Each day was assigned the octant containing the 13 UTC plume heading. For octant k on day t, the column was expressed relative to that day's background, the pixel-weighted mean of the octants at least 90° from the plume:

```
r_{k,t} = X_{k,t} - \bar{X}_{\mathrm{bg},t}
```

The effect in octant k is the mean of r on days when k is downwind minus its mean on days when the plume points at least 90° away. The same pixels appear on both sides of this difference, so fixed geography cancels; subtracting the daily background removes region-wide variation such as Harmattan dust and seasonal burning. An octant enters only with at least five days in each condition, a day only with at least three background octants, and a pixel count of at least three per octant.

Octant effects were averaged per site, weighted by downwind days and pooled over 2019–2024, giving one value per flare or placebo point. Means carry bootstrap 95% CIs over sites, and a one-sided sign test asks whether more than half of the sites are positive. Attribution requires a positive onshore effect, flares exceeding placebo points (one-sided Mann–Whitney), and a placebo effect that is either null or subtracted. Because the placebo effect was not null (Section 4.3), flare effects are reported net of the placebo mean, with a CI from bootstrapping flares and placebo points independently (5,000 resamples). The correlation between each flare's effect and its mean volume (Spearman) is reported as dose–response evidence.

3.7 Regional methane

TROPOMI methane is too sparse for flare-by-flare attribution, so it was analysed at regional scale with the bias-corrected column. The flaring zone was the union of 20 km buffers around all onshore flares active in 2019–2024. For each month, a background surface $XCH_4 = a + b \cdot lat + c \cdot lon$ was fitted to flare-free land pixels in southern Nigeria: at least 50 km from any flare, below 300 m elevation, within 3.8–10° E and 4–8° N, and more than 40 km from central Lagos. The monthly excess is the zone mean minus the surface predicted at the zone. Months were kept when the zone held at least 50 and the background at least 200 pixels, and the mean excess carries a bootstrap 95% CI. Annual excess was compared with onshore flared volume (Spearman).

3.8 Comparison with reported volumes

Satellite volumes were compared with volumes reported by operators to the regulator. The Nigerian Gas Flare Tracker was considered first, because it is Nigeria's official flare-monitoring platform, but it is built on VIIRS detections (Ndunagu et al., 2021); comparing it with the VIIRS Nightfire panel would compare one satellite product with a derivative of itself. It was therefore used only as context. The independent reference is the annual flared volume reported by operators to the Nigerian Upstream Petroleum Regulatory Commission (NUPRC), taken from NUPRC's annual Gas Production Status Reports for 2021, 2023 and 2024 (NUPRC, 2024), in million standard cubic feet (MMscf). The 2022 report on NUPRC's website is incomplete, so the 2022 value is taken from the BudgIT (2026) compilation of NUPRC data; BudgIT's figures match NUPRC's exactly for the three years where both are available. NUPRC marks its October–December 2024 values as provisional. Reported volumes were converted to BCM at 1 MMscf = 2.8317×10^{-5} BCM.

Reported volumes are national totals, whereas the VIIRS panel covers the nine Niger Delta states; flares outside these states carry a small share of national volume (Section 2.2). For each year the satellite-to-reported ratio and the percentage difference were computed, and the year-on-year changes in the two series were compared to ask whether they agree on the direction of change, which matters more for policy than the level. The earlier years (2012–2020) could not be compared because a consistent reported series for those years was not available in a citable form at the time of writing; Section 5.5 discusses the implications.

3.9 Sensitivity analyses

The fixed-sector, placebo-adjusted CO excess was re-estimated under alternative analysis choices, each varied one at a time from the baseline (bold):

- minimum TROPOMI pixels per octant: 1, **3**, 5, 10;

- minimum 100 m wind speed: 1, **2**, 3, 4 m/s;
- minimum downwind and non-plume days per octant: 3, **5**, 10;
- ERA5 wind hour: 12, **13**, 14 UTC (Table S1);
- season: Harmattan dry season (DJF), onset of rains (MAM), peak rains (JJA), late rains (SON);
- leave-one-year-out (six runs, 2019–2024) and leave-one-state-out (Rivers, Delta, Bayelsa, Akwa Ibom; the other states have too few onshore flares to drop individually).

The octant geometry was varied for 2023 only, the year with the best sampling: outer radius 15 and 40 km (baseline 25 km), applied identically to flares and placebo points and compared with the 2023 baseline. A result is called robust if the placebo-adjusted onshore excess stays positive with a 95% CI excluding zero under every choice, and if no single year or state accounts for the sign.

3.10 Supplementary diagnostics

Three further diagnostics use the rotating-sector data. **Distance decay**: downwind pixels were binned at 0–2, 2–5, 5–10 and 10–20 km from the flare, and the mean in each bin was expressed relative to the same-day upwind sector, pooled over site-days. A flare plume should be strongest near the source and fade with distance; a background gradient should do the opposite, growing with distance as the sample moves further inland. **Heterogeneity**: the rotating-sector contrast was summarised by state and by year to see whether the pooled result is driven by one place or one period. **Data availability**: the number of site-days with any downwind pixel, and with both sectors usable (≥ 3 pixels each, wind ≥ 2 m/s), was counted for each gas (Table S2). These diagnostics use the rotating design and are therefore read for their shape, not their level, which Section 4.2 shows is biased.

4 Results

4.1 Flaring trends, 2012–2024

Flared gas in the nine Niger Delta states fell 32%, from 9.69 BCM in 2012 to 6.58 BCM in 2024 (Theil–Sen −0.29 BCM/yr, 95% CI −0.39 to −0.17; Mann–Kendall $\tau = -0.77$, $p < 0.001$; Figure 4). The lowest year was 2022, at 5.41 BCM. The number of active flares did not fall with volume: it stayed between 157 and 186 a year and rose from 164 to 178 ($\tau = 0.20$, $p = 0.36$), so the average flare burned less gas.

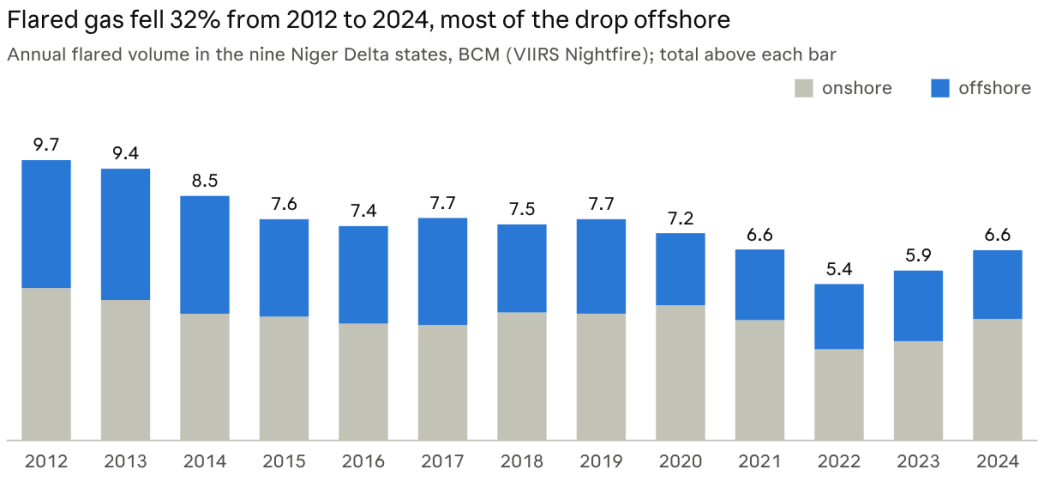

VIIRS Nightfire flare panel, nine Niger Delta states, 2012–2024

Figure 4. Annual flared volume, onshore and offshore.

Offshore flaring fell faster than onshore: 46% (4.43 to 2.38 BCM; −0.19 BCM/yr, $p < 0.001$) against 20% (5.27 to 4.20 BCM; −0.09 BCM/yr, $p = 0.04$), so the offshore share of volume dropped from 46% to 36%. Onshore volume rebounded in 2024, from 3.43 to 4.20 BCM, as 31 new or relit flares appeared, the most of any year. Declines were significant in Rivers, Bayelsa and Akwa Ibom (Table 2).

State	2012 (BCM)	2024 (BCM)	Change	Theil–Sen slope (BCM/yr)	Mann–Kendall p
Rivers	2.81	2.09	−26%	−0.086	< 0.001
Delta	2.56	2.08	−19%	−0.040	0.057
Bayelsa	1.72	0.82	−53%	−0.069	0.002
Akwa Ibom	1.27	0.69	−45%	−0.070	< 0.001
Ondo	0.49	0.16	−67%	−0.022	0.076
Imo	0.42	0.34	−19%	−0.004	0.44
Edo	0.39	0.35	−12%	−0.007	0.16
Abia	0.04	0.05	+21%	−0.002	0.68

Table 2. Flared volume by state (states include their offshore flares), sorted by 2012 volume. No flares were detected in Cross River.

The decline was not uniform across states (Figure 5). Bayelsa (−53%) and Akwa Ibom (−45%), both with a large offshore share, fell furthest, and Rivers fell 26%. Delta fell 19% but without a significant trend, and from 2018 to 2023 it was the largest flaring state, overtaking Rivers. Rivers and Delta together carried 55% of Niger Delta volume in 2012 and 63% in 2024, so flaring is becoming more concentrated in the two states with the most onshore flow stations. Rivers also drove the 2023–2024 rebound, rising 42% from its 2022 low (1.47 to 2.09 BCM). The smaller states contribute little to the total: Ondo fell 67% from a small base, Edo and Imo changed little, and Abia flared under 0.05 BCM in every year.

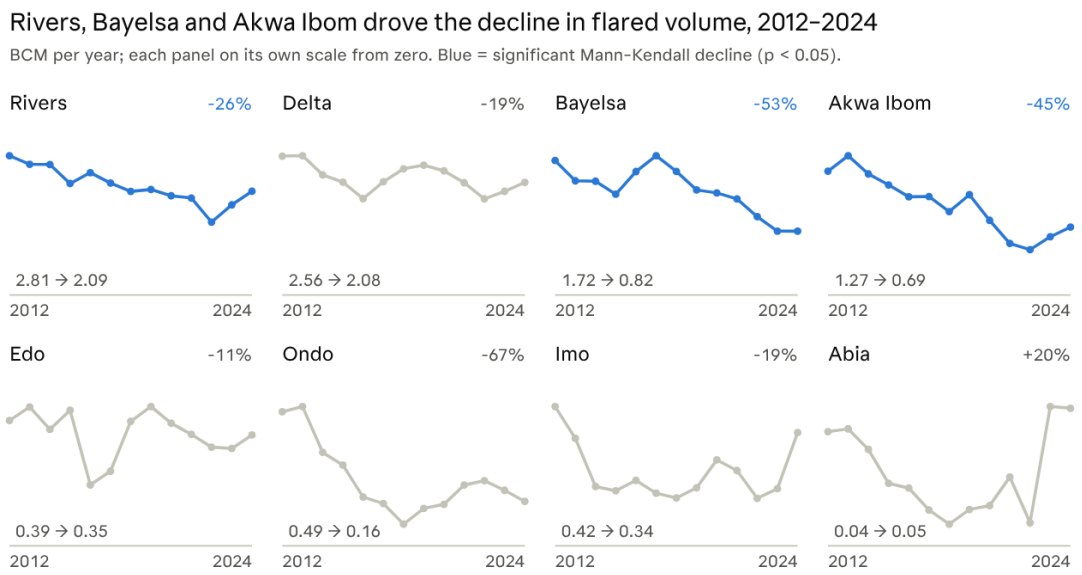

T1_bcm_by_state.csv (VIIRS Nightfire panel) · 8 states × 13 years

Figure 5. Annual flared volume by state, 2012–2024. Each panel has its own vertical scale; the label gives the 2012 and 2024 volumes in BCM and the corner figure the percentage change.

Falling volume did not mean fewer flares (Figure 6). Onshore flares increased from 103 to 133, while offshore flares fell from 61 to 45, so the shift in volume from offshore to onshore was matched by a shift in flare numbers. The mean volume per flare fell 37%, from 0.059 BCM in 2012 to 0.037 BCM in 2024. Most flares persist: in every year from 2013 onward at least 82% of active flares had also been active the previous year, and in 2024 147 of 178 were continuing. Turnover was low before 2016 (five new flares a year) and higher afterwards, peaking at 31 new or relit flares in 2024 and 30 in 2017. Because a flare's identity is defined by a 1 km match across years, a relit flare at an existing station counts as continuing if it was seen the year before and as new if it had been dark for a year or more.

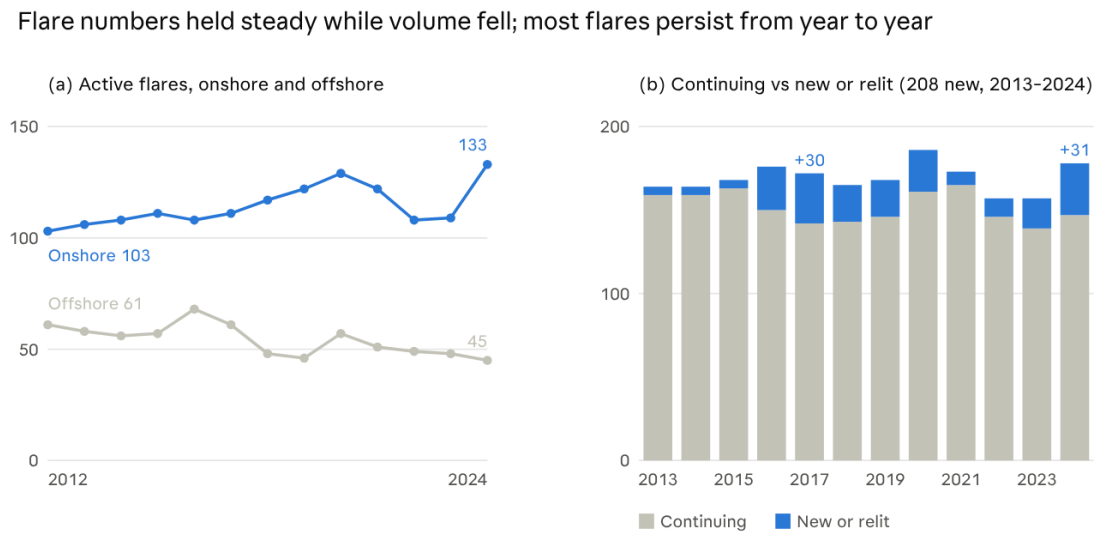

T3_onshore_offshore.csv and T4_flare_dynamics.csv (VIIRS Nightfire panel, persistent site IDs) · 2012–2024

Figure 6. (a) Number of active flares onshore and offshore. (b) Active flares split into those continuing from the previous year and those new or relit; labels mark the two years with the most new flares.

Mapped site by site, the decline was uneven (Figure 7). Of the 164 sites active in 2012, 123 were still flaring in 2024: 86 of them burned less and 37 burned more. Forty-one sites had stopped by 2024, 24 of them offshore, and together they had flared 1.43 BCM in 2012. The 55 sites that appeared after 2012 were mostly onshore (47) and flared 1.23 BCM in 2024, replacing most of the volume lost from stopped sites. A further 91 sites flared only in some years between 2013 and 2023. The net fall of 3.11 BCM therefore came mainly from continuing flares burning less (8.26 to 5.35 BCM), not from flares being shut down.

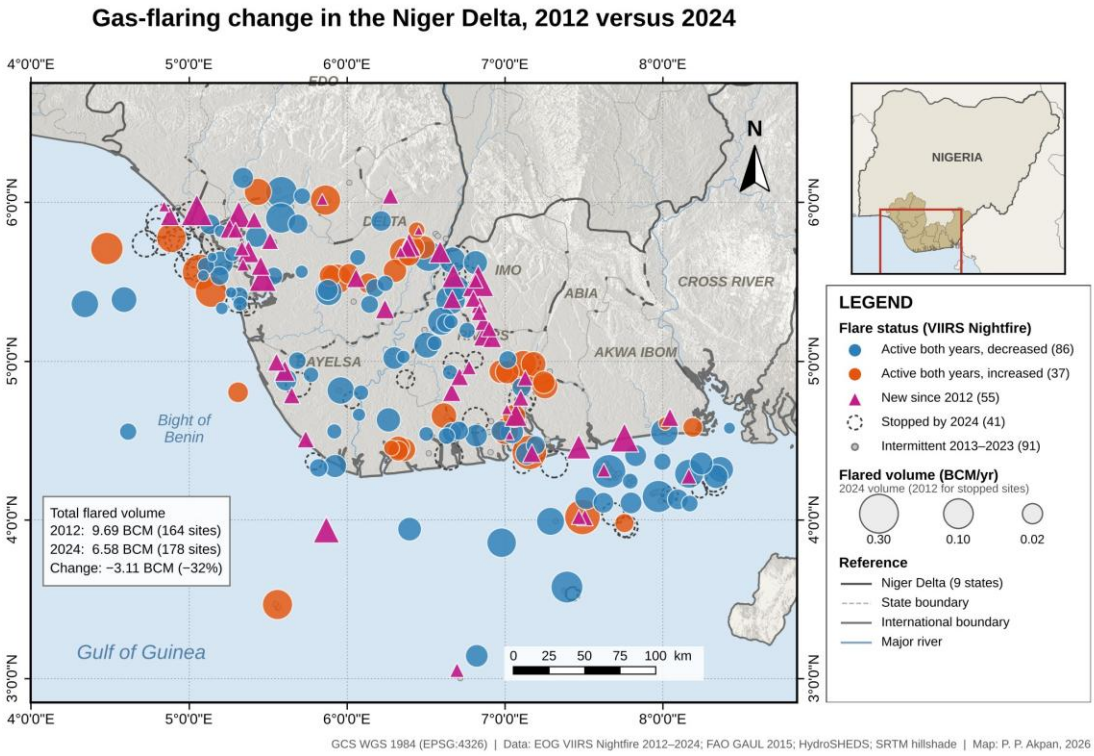

Figure 7. Change in gas flaring between 2012 and 2024 at the 310 persistent VIIRS Nightfire sites. Circles are sized by 2024 volume (2012 volume for stopped sites) and coloured by status: active in both years with lower (blue) or higher (orange) volume, new since 2012 (triangles), stopped by 2024 (dashed circles) and active only between 2013 and 2023 (grey dots). Inset: location within Nigeria.

4.2 Wind-rotated contrasts overstate the flare signal

Downwind of onshore flares, TROPOMI CO exceeded upwind values by 241 µmol/m² (95% CI 185 to 298; 723 flare-years, 174 flares, 2019–2024), but three tests show that most of this contrast is regional structure, not flaring.

The choice of ERA5 hour was not the cause. For the 109 onshore flares of 2023, the contrast was 305, 268 and 255 µmol/m² with winds at 12, 13 and 14 UTC, with overlapping confidence intervals (Table S1). The plume heading moved by a median 7.4° between adjacent hours.

The nulls failed. At the 249 placebo points the same contrast was −151 µmol/m² (95% CI −220 to −82), and 16.2% of point-years were flagged significant against an expected 5%. At the flares themselves, the two crosswind sectors differed by +120 µmol/m² (95% CI 71 to 169), a cross-sector gradient half the size of the apparent signal. Removing a linear gradient left 14 µmol/m² (95% CI −31 to 63), indistinguishable from zero. The within-flare test found no link between a flare's yearly volume and its contrast (p = 0.23), although year-to-year volume changes were small (SD 0.016 BCM). Figure 8 sets the estimate from every design side by side.

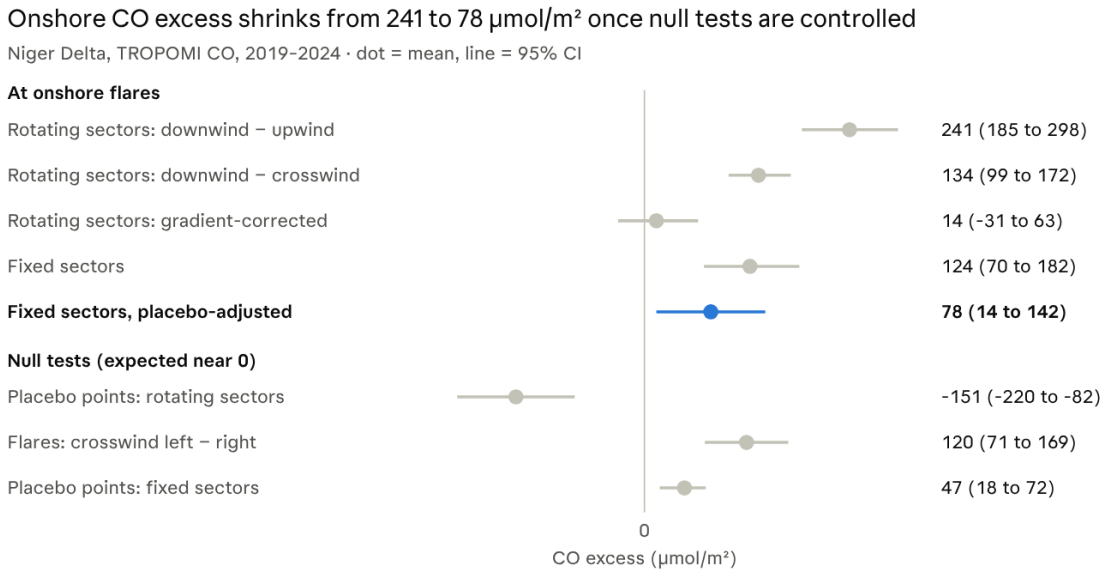

TROPOMI CO, ERA5 13 UTC winds · onshore flares n = 170–174, placebo points n = 249, 2019–2024

Figure 8. Onshore CO excess from every design, applied to the same flares and days. Only the fixed-sector, placebo-adjusted estimate passes both null tests; its sensitivity to analysis choices is shown in Figure 15.

The shape of the onshore CO contrast with distance favours a near-source contribution (Figure 9). Pixels 0–2 km downwind carried +172 µmol/m² above the same-day upwind sector (SE 27), falling to +95 at 2–5 km, +23 at 5–10 km and −104 at 10–20 km. A background gradient alone would produce the opposite pattern, because pixels further downwind lie further inland, where CO is higher. Onshore SO_2 showed the same shape at much lower signal-to-noise: +3.5 µmol/m² (SE 1.4) in the nearest band, close to zero at 2–5 km and negative beyond, the only evidence of a flare-linked SO_2 signal in this study. Offshore, the CO contrast was negative in every band and most negative next to the flare (−644 µmol/m² at 0–2 km), rising toward zero with distance. Offshore flares are seen against a sea surface where TROPOMI CO retrievals behave differently from those over land, and their downwind sector reaches the coast on monsoon days, so the offshore pattern reflects the land–sea contrast rather than the flares.

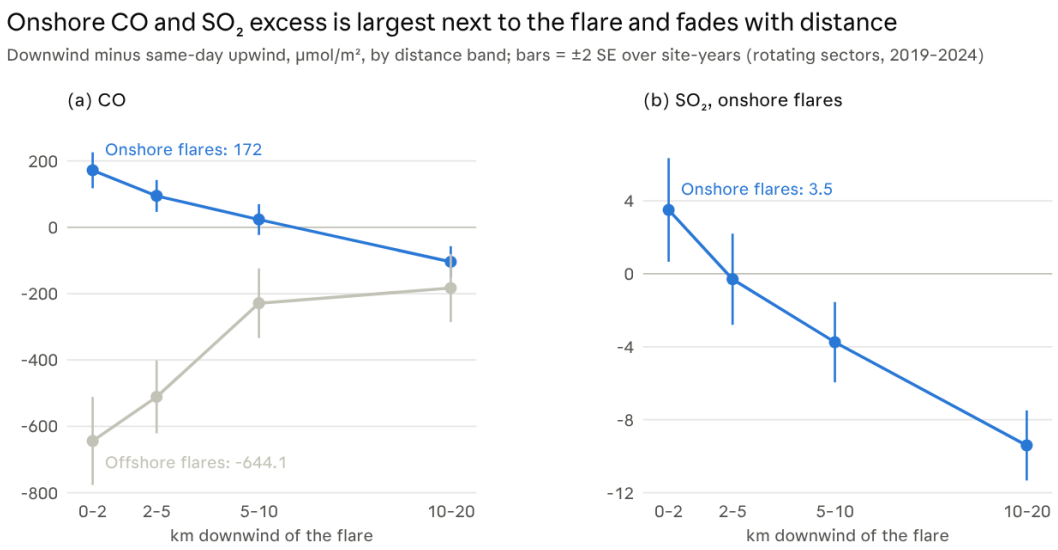

A5_distance_decay_pooled.csv (TROPOMI CO and SO_2, ERA5 13 UTC) · 723 onshore and 296 offshore site-years

Figure 9. Downwind CO (a) and SO_2 (b) excess relative to the same-day upwind sector, by distance from the flare, pooled over site-years 2019–2024. Points are means; bars show ±2 standard errors.

The rotating contrast was positive in the states whose flares are mostly onshore and negative where flares are mostly offshore or coastal (Figure 10a): Rivers +286 µmol/m² (69% of 284 site-years positive) and Delta +221 (70% of 331), against Bayelsa −6, Akwa Ibom −165 and Ondo −438. Abia (+475) and Edo (+129) were positive but rest on 7 and 36 site-years. By year (Figure 10b) the contrast was positive in all six years, smallest in 2019 (+42; the first year, with coarser 7 × 7 km pixels before August) and largest in 2020–2021 (+230 and +217). No single state or year carries the onshore result, but the split by state repeats the onshore–offshore split already seen in Figure 9, and these values carry the rotating design's bias described above.

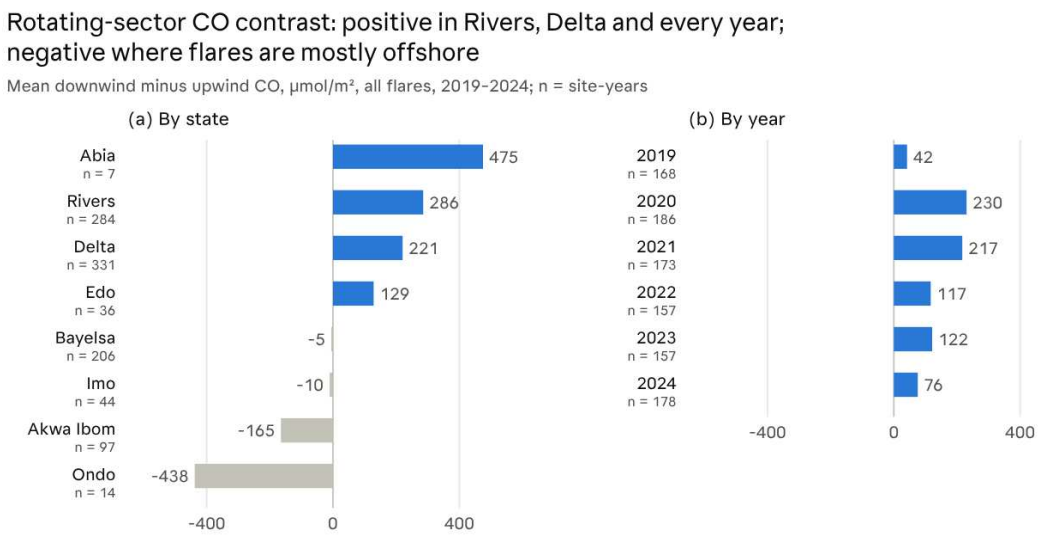

A3_pooled_enhancement.csv (TROPOMI CO, rotating sectors, ERA5 13 UTC) · 1,019 site-years

Figure 10. Mean rotating-sector CO contrast (downwind minus upwind) by state (a) and year (b), all flares, with the number of site-years. Blue bars are positive, grey negative.

4.3 Fixed-sector CO and SO_2 at flare sites

With fixed compass sectors, onshore flares carried a placebo-adjusted CO excess of 78 µmol/m² (95% CI 14 to 142), about one third of the wind-rotated contrast. Onshore flares averaged 124 µmol/m² (95% CI 70 to 182; 60% of 170 flares positive, sign test p = 0.006) and exceeded the placebo points (one-sided Mann–Whitney p = 0.014). The placebo points were not null under this design either: +47 µmol/m² (95% CI 18 to 72; 59% of 249 points positive). Because fixed sectors cancel static geography, this residual is wind-linked, and it is subtracted rather than ignored (Table 3).

Fixed-sector CO effect (µmol/m²)	Sites	Mean	95% CI	Sites positive
Onshore flares	170	124	70 to 182	60%
Offshore flares	63	−72	−193 to 53	46%
Placebo points	249	47	18 to 72	59%
Onshore flares, placebo-adjusted	170 vs 249	**78**	**14 to 142**	—

Table 3. Fixed-sector CO effects, one value per site, 2019–2024.

The onshore effect did not scale with mean flared volume (Spearman ρ = 0.00, p = 0.96). Offshore flares showed no excess, and SO_2 showed no flare signal in any design: onshore −4.5 µmol/m² (95% CI −7 to −2) against placebo −0.8 (−3 to 1).

The site-level effects behind Table 3 are mapped in Figure 11. The onshore excess is spread across the flaring belt rather than carried by a few sites. It was positive on average in Delta (mean +149 µmol/m²,

66 sites) and Rivers (+137, 47 sites), where 11 of the 15 onshore sites above +600 lie, and negative in Bayelsa (−152, 29 sites), the same split by state as the rotating design (Figure 10). Offshore sites are mixed in sign. Single-site effects are noisy, ranging from about −1,000 to +1,300 µmol/m² onshore, so the map shows where the pooled signal comes from, not which individual flares are significant.

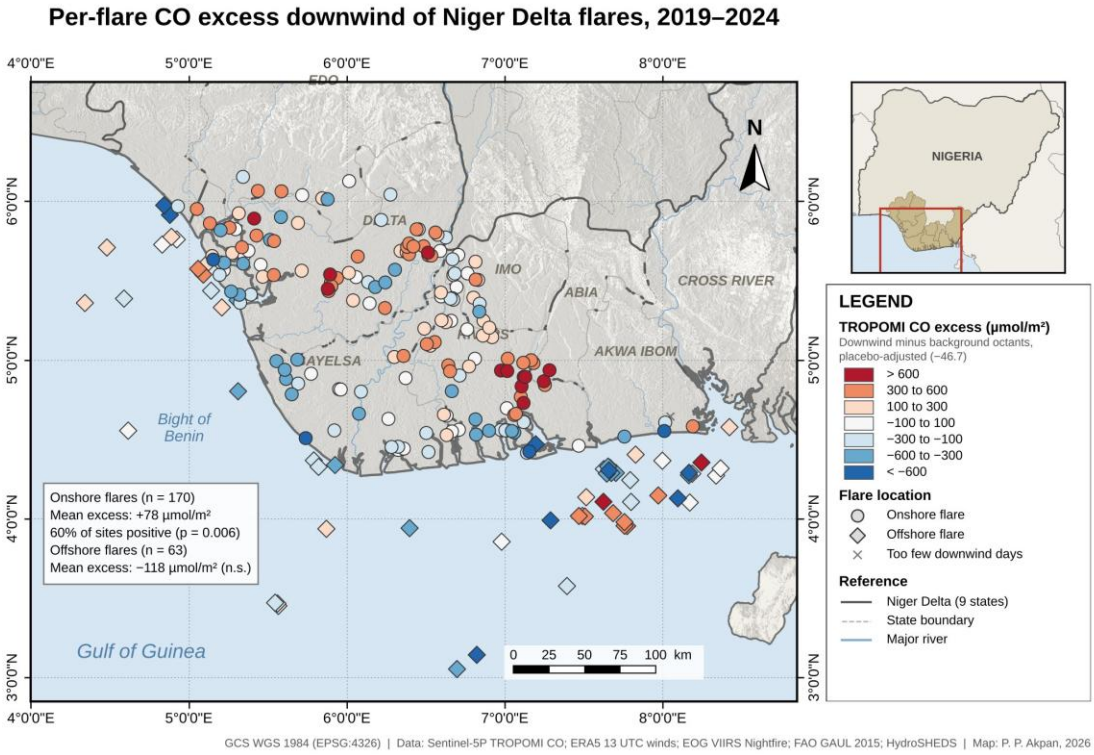

Figure 11. Placebo-adjusted CO excess at each flare: the downwind octant minus the background octants, less the placebo mean of 46.7 µmol/m², TROPOMI 2019–2024. Circles are onshore flares (n = 170) and diamonds offshore flares (n = 63); crosses mark four sites with too few downwind days. Inset: location within Nigeria.

4.4 Regional methane over the flaring zone

Bias-corrected XCH_4 over the onshore flaring zone exceeded the latitude- and longitude-adjusted background by +5.3 ppb (median +7.7; 95% CI 2.4 to 8.1), positive in 17 of 21 well-sampled months. The uncorrected product gave +8.8 ppb, so about 40% of that excess came from the retrieval's albedo dependence. The background surface fell by 2.9 ppb per degree north. The excess was largest in the late rains (September–November, +12.5 ppb, 4 months) and smaller in the Harmattan season (December–February, +4.3 ppb, 15 months); the peak-rain months had too few cloud-free pixels. Annual excess was not correlated with onshore flared volume (Spearman ρ = 0.03, n = 6 years).

Only 21 of 71 months between February 2019 and December 2024 had enough clear-sky XCH_4 retrievals both inside the flaring zone and in the background to be used, and none of them fell in June–September (Figure 12). Fifteen of the 21 were Harmattan months (December–February), when dry north-easterly air clears the cloud. The excess was positive in 17 of the 21 months, with a mean of 5.3 ppb; it averaged 4.3 ppb in the Harmattan months and 12.5 ppb in the four November and October months, while the two April months averaged −1.6 ppb. A spatial regression across 918 grid cells, with latitude and

longitude as covariates, found no relation between XCH_4 and the volume flared within 20 km (−4.0 ppb per BCM/yr; block-bootstrap 95% CI −12.3 to 5.4; p = 0.34; R^2 = 0.60, almost all from latitude). The methane excess is therefore regional: it marks the flaring zone as a whole but cannot be tied to individual flares or to how much they burn.

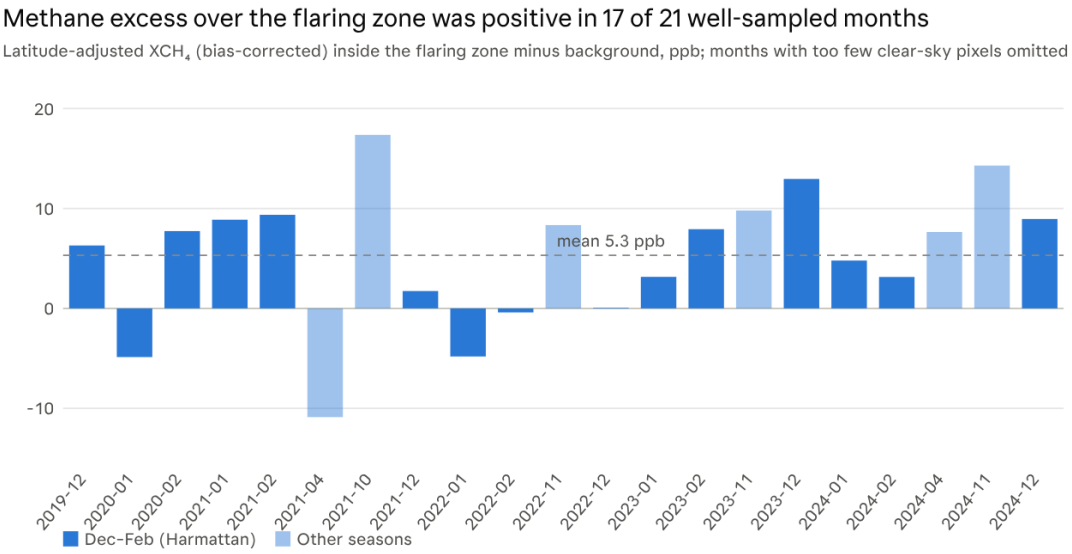

M6_monthly_dXCH4_latitude_adjusted.csv (TROPOMI XCH_4 bias-corrected) · 21 well-sampled months of 71, Dec 2019–Dec 2024

Figure 12. Monthly latitude-adjusted methane excess over the flaring zone in the 21 well-sampled months, 2019–2024. Darker bars are Harmattan months; the dashed line is the mean.

Averaged over all November–February retrievals on a 0.1° grid, the same regional picture appears (Figure 13). Cells inside the 20 km flaring zone averaged +6.3 ppb (median +4.9 ppb) above a background surface fitted to land cells more than 50 km from any flare. The anomaly is highest over southern Delta, Bayelsa and western Rivers, but positive cells also extend north along the lower Niger, well outside the flaring zone, and parts of the zone around Port Harcourt are close to zero. The composite is close to the monthly mean of 5.3 ppb; the difference comes from pooling every retrieval rather than weighting each month equally.

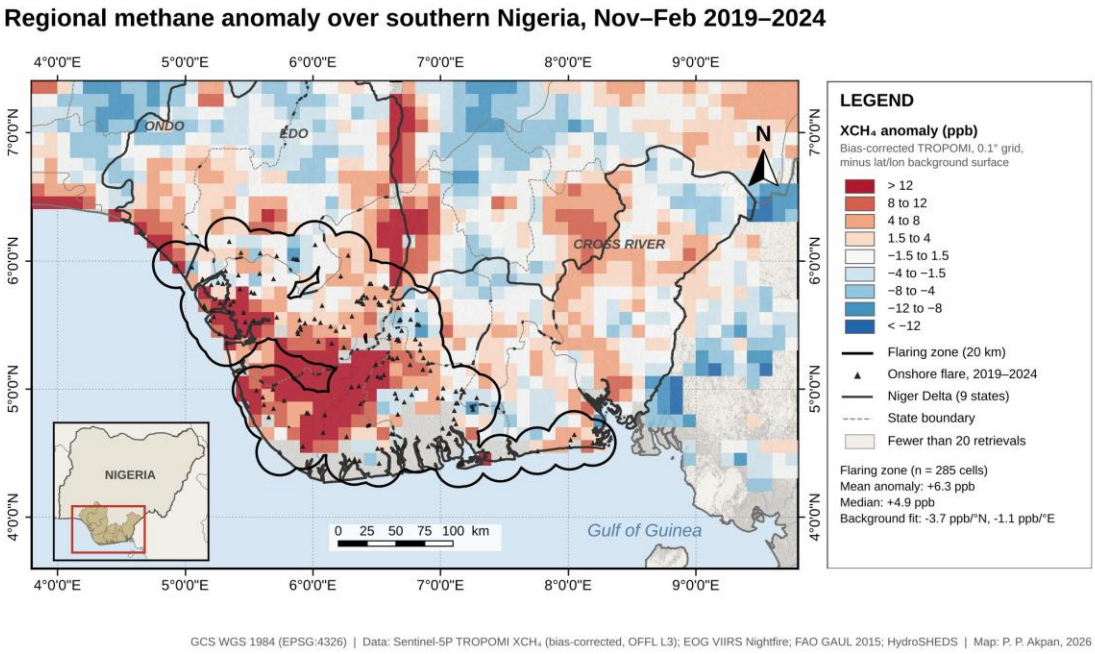

Figure 13. Bias-corrected TROPOMI XCH_4 anomaly, November–February 2019–2024, on a 0.1° grid: the mean column minus a background surface in latitude and longitude fitted to land cells at least 50 km from any flare. Cells with fewer than 20 retrievals are left blank. The black outline is the flaring zone (20 km around onshore flares active in 2019–2024). Inset: location within Nigeria.

4.5 Satellite versus reported volumes

Over 2021–2024, VIIRS put Niger Delta flaring at 24.5 BCM and operators reported 23.1 BCM nationally, a difference of 5.7% (Figure 14). The agreement was close in 2021 (VIIRS 7.7% lower) and 2022 (1.3% higher) but diverged afterwards: VIIRS was 13.0% higher in 2023 and 20.4% higher in 2024. The two series agreed on the direction of change in 2022 (VIIRS −18.1%, reported −25.4%) and 2024 (+12.0% and +5.1%) but not in 2023, when VIIRS rose 8.6% and reported volumes fell 2.6%. Because VIIRS here excludes flares outside the nine states, the true national gap in 2023–2024 is, if anything, slightly larger. The VIIRS rise in 2023–2024 coincides with the jump in new and relit onshore flares (Figure 6) and with Rivers' rebound (Figure 5), so the divergence is concentrated where new flares appeared. Table 4 sets out the reference datasets and why only one of them is independent of VIIRS.

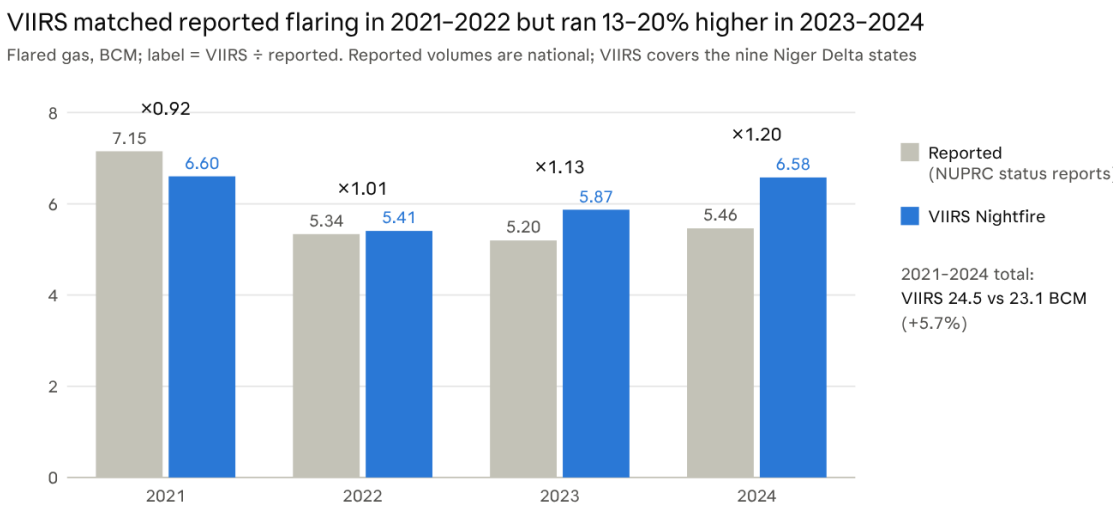

Reported: NUPRC Gas Production Status Reports 2021, 2023, 2024 (2022 via BudgIT, 2026), MMscf; satellite: T1_bcm_by_state.csv (VIIRS Nightfire) · 2021–2024

Figure 14. Annual flared volume reported by operators to NUPRC (national) and estimated by VIIRS Nightfire (nine Niger Delta states), 2021–2024. The label above each pair is the VIIRS-to-reported ratio.

Dataset	Basis	Spatial unit	Independent of VIIRS?	Used here
VIIRS Nightfire site files (EOG/World Bank)	Satellite radiant heat, calibrated to reported volumes	Flare site, annual	—	Panel and trends (Sections 4.1–4.4)
Nigerian Gas Flare Tracker (NOSDRA)	VIIRS detections converted to volume	Flare site, monthly	No	Context only
NUPRC Gas Production Status Reports (NUPRC, 2024; 2022 via BudgIT, 2026)	Metered or estimated by operators	National, by company	Yes	Comparison, 2021–2024
World Bank GGFR country totals	VIIRS, same calibration	Country, annual	No	Not used

Table 4. Reference datasets for Nigerian flared volumes.

4.6 Sensitivity of the CO estimate

The ERA5 wind hour made little difference (Section 4.2; Table S1). The other choices mattered more, and by the criterion set in Section 3.9 the fixed-sector estimate is not robust (Figure 15; Table S3).

The estimate was stable to the pixel threshold (76–100 µmol/m², all CIs above zero), to a stricter day threshold (93), and to leaving out Bayelsa (125) or Akwa Ibom (87). It was not stable in three respects.

First, it depends on season: the Harmattan months (December–February) gave 229 µmol/m² (95% CI 66 to 394), while the other three seasons were each close to zero or negative with CIs spanning zero. Second, it depends on wind speed: admitting days down to 1 m/s lowered it to 45 (CI −23 to 105), and restricting to days of at least 3 or 4 m/s reversed its sign (−171 and −255). Third, it depends on Rivers and Delta: leaving out either state, or the years 2020 or 2022, moved the lower CI bound below zero.

Two of these patterns are expected for a real point source. A flare's column enhancement scales inversely with wind speed, so it should be strongest on calm days and fade as wind increases; and the Harmattan is the clearest season, with the most TROPOMI CO retrievals of good quality and north-easterly flow that carries onshore plumes toward the coast instead of inland. The sign reversal at higher winds is not expected. It shows that a wind-linked background structure, of opposite sign to the flare signal, remains after placebo adjustment on windy days, when the placebo sample also thins (to 67 points at 4 m/s). The 78 µmol/m² baseline is therefore best read as an average over conditions, carried by Harmattan, light-wind days in Rivers and Delta, rather than as a year-round flare signal.

The sector-radius test was run for 2023 only, the best-sampled year, and with a three-day minimum per octant because one year gives fewer days. In that year alone the 25 km baseline was not significant (−79 µmol/m², 95% CI −236 to 68), consistent with 2023 being the year whose removal raised the pooled estimate most (Figure 15). Within that year, the radius moved the estimate in the direction a near-source signal predicts: shrinking the sectors to 15 km raised it to +14 (−93 to 121), while widening them to 40 km lowered it to −167 (−318 to −12). Wider sectors sample more of the regional background that the distance-decay analysis showed to be negative beyond 10 km (Figure 9), and dilute the flare's near-field contribution, so the geometry test points the same way as the distance decay. No single-year radius choice produced a significant positive excess, however, so the pooled multi-year estimate rests on the Harmattan months across years, not on any one year.

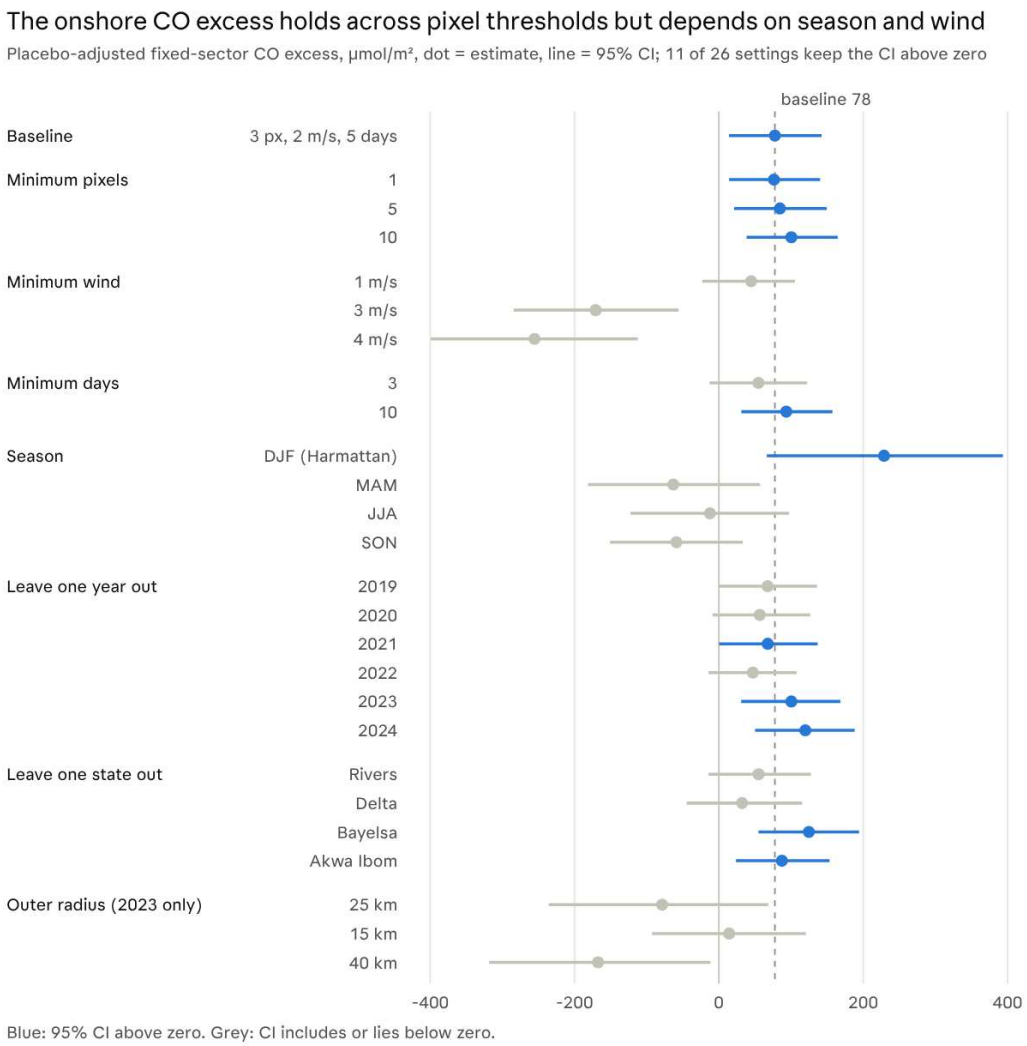

S1_sensitivity_thresholds_season_loo.csv and S2_sensitivity_geometry_2023.csv (Colab cells 6.1–6.4) · 26 settings, 2019–2024

Figure 15. Sensitivity of the placebo-adjusted onshore CO excess to analysis choices. Each row changes one choice from the baseline; the dashed line marks the baseline estimate. Full values are in Table S3.

5 Discussion

5.1 What the falsification layer changed

Without the null tests, the onshore CO excess would have been reported about three times too large (Figure 8). In the Niger Delta, CO varies from the coast inland and with land cover, settlement and burning, so a sector that turns with the wind samples different ground on different days. Under the persistent south-westerly monsoon, the downwind sector of a flare lies mostly inland and the upwind sector mostly toward the coast. A coast-to-inland gradient therefore appears as a downwind excess at every flare, while the placebo points, mostly north of the flaring zone, sit on a different part of that

gradient and returned a negative contrast. The crosswind null and the gradient-corrected estimator exposed this from the flare data alone, at no extra cost. Fixed sectors removed the static part of it.

The fixed-sector placebo residual (+47 μmol/m²) shows that not all of the artefact is static. A likely cause is that wind direction is correlated with the air mass: when the wind blows toward a given octant, regional CO carried on the same flow can raise that octant relative to the others. Subtracting the placebo mean removes this to the extent that flares and placebo points share it. We recommend that sector-based point-source studies report a placebo contrast and a crosswind null beside every flare estimate, and treat an estimate that fails them as an upper bound.

5.2 Interpreting the CO excess at onshore flares

The placebo-adjusted excess of 78 μmol/m² shows that onshore flare sites are CO hotspots, but not that flaring alone causes it. The excess did not scale with VIIRS flared volume, and flare sites in the Delta sit among other combustion sources: artisanal refineries, generators, road traffic and open burning. Variable combustion efficiency would also weaken the link between volume and CO (Plant et al., 2022). We therefore report an enhancement associated with flare sites, not an emission factor for flaring.

The flare-attributable excess did not scale with flared volume under any design (fixed-sector Spearman $\rho = 0.00$; rotating-sector $\rho = -0.01$, $p = 0.83$). Four explanations are compatible with this. First, the volumes themselves compress the true range: Zhizhin et al. (2021) showed that Nightfire underestimates the largest flares, which are more often hidden by cloud and smoke, and overestimates small, persistent ones, whose frequent detections inflate their annual sum; both errors flatten any dose–response. Second, CO is a product of incomplete combustion, so it tracks combustion efficiency rather than volume. A large, well-aerated flare can emit less CO than a small, smoky one burning wet or liquid-rich gas, and Niger Delta flares range from elevated stacks to horizontal ground-level pits. Third, a TROPOMI pixel of about 19 km² averages a flare plume with everything else in it, and with retrieval noise of the same order as the excess, single-site effects are noisy enough to hide a weak gradient across sites. Fourth, flares share their surroundings with other combustion sources whose activity does not follow flared volume: flow-station generators, gas turbines, traffic on new roads, and, in Rivers and Bayelsa especially, artisanal crude refining, which burns crude oil in open pits. The distance decay (Figure 9) shows that something near the flare raises CO; it cannot say whether it is the flare alone.

5.3 Null results for SO_2 and offshore CO

SO_2 from individual flares appears to lie below what TROPOMI can resolve: the SO_2 point sources detected from space are generally large industrial and volcanic emitters (Fioletov et al., 2016). Offshore, few platforms had enough downwind days in each octant, and TROPOMI CO over water is retrieved mostly in cloudy scenes, where sensitivity to the surface layer is low.

5.4 Methane

The bias-corrected excess of 5.3 ppb is a regional enhancement over the flaring zone. Wetlands and mangroves are strong natural methane sources in the Delta, and the excess did not track flared volume. It is consistent with persistent oil-and-gas methane emissions in the region, from venting, leaks and incomplete combustion (Plant et al., 2022; Lauvaux et al., 2022), without isolating flaring. Using the bias-corrected product mattered: it removed about 40% of the excess estimated from the uncorrected column.

5.5 Satellite and reported volumes

The 5.7% agreement between VIIRS and operator-reported volumes over 2021–2024 should not be read as independent validation of the level. Nightfire volumes are calibrated against country-reported volumes worldwide (Elvidge et al., 2016), so close national agreement in some years is partly built in. What the comparison can test is change over time, and there the series diverged: from 2022 to 2024 VIIRS rose 22% while reported volumes rose 2%, so that by 2024 satellites saw 1.12 BCM (about 39,400 MMscf) more than operators reported. At the US$2.00 per thousand scf penalty of the 2018 Regulations, that gap is worth roughly US$79 million in a single year. The divergence is concentrated in the onshore states where new and relit flares appeared (Figures 5 and 6).

Three explanations are possible, and the data here cannot choose between them. Operators may under-report, as field-level comparisons have found for some offshore fields (Ndunagu et al., 2021). Flares may be operated by companies that report late or not at all, a risk that grows as onshore assets pass from international to Nigerian operators and to marginal-field holders. Or VIIRS may over-count, if the new detections include artisanal refining fires or other hot sources classified as flares, or if more frequent detection in clearer years inflates the annual sum (Zhizhin et al., 2021). Distinguishing these needs a site-level match between the VIIRS panel and company-reported volumes, which the NUPRC data published by company make possible, and a reported series back to 2012. The Nigerian Gas Flare Tracker cannot settle the question, because it is itself derived from VIIRS.

5.6 Implications for monitoring in Nigeria

Three practical points follow. First, flared volume and air-quality impact are different quantities. A 32% fall in volume since 2012 has not been matched by fewer flares: the number of onshore flares rose, and the CO contrast around flares was no smaller in 2024 than in 2019. Policy targets framed only in volume, such as Zero Routine Flaring, can be met on paper while flares near communities continue to burn. Monitoring should report flare counts and onshore locations alongside volume. Second, satellite trace-gas data can support that monitoring, but only with falsification built in. The rotating-sector method that is standard in the literature would have tripled the onshore CO estimate here; a regulator using it would overstate impacts and invite challenge. The placebo and fixed-sector tests used in this study are inexpensive, require no new data, and can be run routinely. Third, reported and satellite volumes should be reconciled every year at site level. Divergence of 13–20% in 2023–2024 is large enough to matter for penalties and for the Nigerian Gas Flare Commercialisation Programme, which allocates flare sites to investors based on their volumes. NOSDRA, NUPRC and the Nigerian Gas Flare Tracker together already hold the data needed to do so.

5.7 Limitations

- The +47 µmol/m² placebo residual was subtracted; its cause is inferred, not demonstrated.
- TROPOMI's 5.5 × 7 km pixels blur the 2–25 km near-field around each flare.
- The persistent monsoon leaves some octants with few downwind days.
- Flared volume varies little within a flare from year to year, limiting dose–response tests.
- VIIRS volumes are estimates from radiant heat, not metered flows (Elvidge et al., 2016).
- The fixed-sector CO excess is not robust to all analysis choices. It is concentrated in December–February and on light-wind days, and it reverses sign on days with winds of 3 m/s or more, which shows a residual wind-linked background that the placebo adjustment does not fully

remove (Section 4.6). A design that models the background explicitly, for example with a regression on wind speed, direction and season at placebo points, would be a natural next step.

6 Conclusions

Flared gas in the Niger Delta fell by a third between 2012 and 2024, mostly offshore, even as onshore flares became more numerous, and in 2023–2024 satellites saw 13–20% more flaring than operators reported. Around onshore flares, TROPOMI detected a CO excess of 78 µmol/m² that was largest next to the flares and decreased with distance, and methane was enhanced by 5.3 ppb over the flaring zone. These results hold only because the background was tested: a conventional wind-rotated contrast would have reported 241 µmol/m², about three times the flare-attributable signal. Placebo points, crosswind controls and fixed sectors are cheap, use only data already in hand, and should be standard in satellite source attribution wherever backgrounds are heterogeneous.

The main conclusions are:

1. Niger Delta flaring fell 32% in volume from 2012 to 2024, driven by Bayelsa, Akwa Ibom and Rivers and by offshore flares, but the number of onshore flares rose from 103 to 133 and the mean volume per flare fell 37%. Flaring is becoming smaller, more numerous onshore, and more concentrated in Rivers and Delta.
2. Wind-rotated downwind-minus-upwind contrasts overstated the onshore CO signal about threefold. Placebo points and crosswind sectors revealed this from the data alone.
3. With fixed sectors and placebo adjustment, onshore flare sites carried a CO excess of 78 µmol/m², largest within 2 km of flares and decreasing with distance. It did not scale with VIIRS volume, consistent with known biases in Nightfire volumes and with CO depending on combustion efficiency. Its size depends on season and wind speed (Figure 15): it is clearest in the Harmattan and on light-wind days, so it is best read as a dry-season detection rather than a year-round flux.
4. Methane was enhanced regionally by about 5 ppb, but TROPOMI XCH_4 over the Delta is too sparse, at 21 usable months in six years, to resolve individual flares.
5. VIIRS and operator-reported volumes agreed within 6% over 2021–2024 but diverged by 13–20% in 2023–2024. Annual site-level reconciliation of the two, which the Nigerian Gas Flare Tracker cannot provide because it is VIIRS-derived, would strengthen enforcement of Nigeria's flaring regulations.

Data and code availability

TROPOMI Level-3 CO, SO_2 and CH_4 (COPERNICUS/S5P/OFFL), ERA5 hourly winds (ECMWF/ERA5/HOURLY), the Hansen Global Forest Change data mask, SRTM elevation, ESA WorldCover and FAO GAUL boundaries were accessed through Google Earth Engine. VIIRS Nightfire flare detections were obtained from the Earth Observation Group, Colorado School of Mines, under its data use licence and cannot be redistributed; derived flare panels are available on request within the licence terms. The Colab notebook that reproduces every analysis, table and figure will be deposited with a DOI on acceptance [DOI].

Operator-reported flared volumes for 2021–2024 are taken from NUPRC's Gas Production Status Reports (NUPRC, 2024), with 2022 from BudgIT (2026). Part 6 of the notebook (cells 6.1–6.4) reproduces the sensitivity analyses in Figure 15 and Table S3.

CRediT authorship contribution statement

Progress Peter Akpan: Conceptualization, Methodology, Software, Formal analysis, Data curation, Visualization, Writing – original draft.

Declaration of generative AI and AI-assisted technologies in the writing process

During the preparation of this work the author used Claude (Anthropic) to review and revise analysis code and to draft and edit text. After using this tool, the author reviewed and edited the content as needed and takes full responsibility for the content of the publication.

Declaration of competing interest

The author declares no known competing financial interests or personal relationships that could have appeared to influence the work reported in this paper.

Acknowledgements

The author thanks the Earth Observation Group, Colorado School of Mines, for VIIRS Nightfire data; the European Space Agency and Copernicus programme for Sentinel-5P TROPOMI data; ECMWF and the Copernicus Climate Change Service for ERA5; and Google for Earth Engine. This research received no specific grant from funding agencies in the public, commercial or not-for-profit sectors.

Supplementary material

ERA5 hour (UTC)	Onshore flares	Mean downwind − upwind CO (µmol/m²)	95% CI	Flare-years significant
12	109	305	208 to 401	31%
13	109	268	178 to 361	31%
14	109	255	157 to 349	37%

Table S1. Sensitivity of the 2023 onshore CO contrast to the ERA5 wind hour. Median heading change between adjacent hours 7.4°; heading left the 22.5° half-width on 15–16% of days.

Gas	Site-days with any downwind pixel	Any upwind pixel	Both sectors ≥ 3 px	…and wind ≥ 2 m/s (usable)	Median downwind pixels
CO	220,098	205,987	178,736	125,985	178
SO_2	218,727	219,195	189,205	129,812	184

Gas	Site-days with any downwind pixel	Any upwind pixel	Both sectors ≥ 3 px	…and wind ≥ 2 m/s (usable)	Median downwind pixels
CH_4	6,153	6,701	3,915	2,092	82

Table S2. TROPOMI data availability for the rotating-sector design, all flares, 2019–2024. Methane has about 1.7% of the usable site-days of CO, which is why it is analysed regionally (Section 3.7).

Choice varied	Setting	Placebo-adjusted onshore CO excess, µmol/m² (95% CI)	Onshore flares / placebo points
Baseline	3 px, 2 m/s, 5 days, 13 UTC, 2–25 km	78 (14 to 142)	170 / 249
Minimum pixels	1	76 (14 to 140)	170 / 249
	5	85 (21 to 149)	170 / 249
	10	100 (38 to 165)	170 / 249
Minimum wind speed	1 m/s	45 (−23 to 105)	174 / 249
	3 m/s	−171 (−284 to −56)	160 / 239
	4 m/s	−255 (−399 to −112)	125 / 67
Minimum days per octant	3	55 (−13 to 122)	174 / 249
	10	93 (31 to 157)	165 / 249
Season	DJF (Harmattan)	229 (66 to 394)	159 / 249
	MAM	−63 (−181 to 57)	155 / 239
	JJA	−12 (−123 to 97)	147 / 249
	SON	−59 (−151 to 33)	156 / 249
Leave one year out	2019	68 (0 to 136)	166 / 249
	2020	57 (−9 to 127)	168 / 249
	2021	68 (0 to 137)	168 / 249
	2022	47 (−14 to 108)	168 / 249

Choice varied	Setting	Placebo-adjusted onshore CO excess, µmol/m² (95% CI)	Onshore flares / placebo points
	2023	100 (31 to 168)	168 / 249
	2024	120 (50 to 188)	152 / 249
Leave one state out	Rivers	55 (−15 to 128)	123 / 249
	Delta	32 (−45 to 115)	104 / 249
	Bayelsa	125 (55 to 194)	141 / 249
	Akwa Ibom	87 (24 to 153)	166 / 249
Outer radius (2023)	25 km (2023 baseline) / 15 km / 40 km	−79 (−236 to 68) / 14 (−93 to 121) / −167 (−318 to −12)	

Table S3. Sensitivity of the fixed-sector, placebo-adjusted onshore CO excess. Each row changes one choice from the baseline.

References

- Abadie, A., Diamond, A., Hainmueller, J., 2010. Synthetic control methods for comparative case studies: Estimating the effect of California's tobacco control program. Journal of the American Statistical Association 105(490), 493–505. https://doi.org/10.1198/jasa.2009.ap08746
- Anejionu, O.C.D., Whyatt, J.D., Blackburn, G.A., Price, C.S., 2015a. Contributions of gas flaring to a global air pollution hotspot: Spatial and temporal variations, impacts and alleviation. Atmospheric Environment 118, 184–193. https://doi.org/10.1016/j.atmosenv.2015.08.006
- Anejionu, O.C.D., Blackburn, G.A., Whyatt, J.D., 2015b. Detecting gas flares and estimating flaring volumes at individual flow stations using MODIS data. Remote Sensing of Environment 158, 81–94. https://doi.org/10.1016/j.rse.2014.11.018
- Beirle, S., Boersma, K.F., Platt, U., Lawrence, M.G., Wagner, T., 2011. Megacity emissions and lifetimes of nitrogen oxides probed from space. Science 333(6050), 1737–1739. https://doi.org/10.1126/science.1207824
- Beirle, S., Borger, C., Dörner, S., et al., 2019. Pinpointing nitrogen oxide emissions from space. Science Advances 5(11), eaax9800. https://doi.org/10.1126/sciadv.aax9800
- Borsdorff, T., aan de Brugh, J., Hu, H., et al., 2018. Measuring carbon monoxide with TROPOMI: First results and a comparison with ECMWF-IFS analysis data. Geophysical Research Letters 45(6), 2826–2832. https://doi.org/10.1002/2018GL077045
- Böttcher, K., Paunu, V.-V., Kupiainen, K., et al., 2021. Black carbon emissions from flaring in Russia in the period 2012–2017. Atmospheric Environment 254, 118390. https://doi.org/10.1016/j.atmosenv.2021.118390
- Brandt, A.R., 2020. Accuracy of satellite-derived estimates of flaring volume for offshore oil and gas operations in nine countries. Environmental Research Communications 2(5), 051006. https://doi.org/10.1088/2515-7620/ab8e17

- BudgIT, 2026. Nigeria's Gas Flaring Crisis in Numbers. BudgIT Foundation, Lagos. https://budgit.org/wp-content/uploads/2026/08/Nigerias-Gas-Flaring-Crisis-in-Numbers.pdf
- Cameron, A.C., Gelbach, J.B., Miller, D.L., 2008. Bootstrap-based improvements for inference with clustered errors. Review of Economics and Statistics 90(3), 414–427. https://doi.org/10.1162/rest.90.3.414
- Casadio, S., Arino, O., Serpe, D., 2012. Gas flaring monitoring from space using the ATSR instrument series. Remote Sensing of Environment 116, 239–249. https://doi.org/10.1016/j.rse.2010.11.022
- Caseiro, A., Gehrke, B., Rücker, G., Leimbach, D., Kaiser, J.W., 2020. Gas flaring activity and black carbon emissions in 2017 derived from the Sentinel-3A Sea and Land Surface Temperature Radiometer. Earth System Science Data 12(3), 2137–2155. https://doi.org/10.5194/essd-12-2137-2020
- de Gouw, J.A., Veefkind, J.P., Roosenbrand, E., et al., 2020. Daily satellite observations of methane from oil and gas production regions in the United States. Scientific Reports 10, 1379. https://doi.org/10.1038/s41598-020-57678-4
- Efron, B., 1979. Bootstrap methods: Another look at the jackknife. Annals of Statistics 7(1), 1–26. https://doi.org/10.1214/aos/1176344552
- Elvidge, C.D., Ziskin, D., Baugh, K.E., et al., 2009. A fifteen year record of global natural gas flaring derived from satellite data. Energies 2(3), 595–622. https://doi.org/10.3390/en20300595
- Elvidge, C.D., Zhizhin, M., Hsu, F.-C., Baugh, K.E., 2013. VIIRS Nightfire: Satellite pyrometry at night. Remote Sensing 5(9), 4423–4449. https://doi.org/10.3390/rs5094423
- Elvidge, C.D., Zhizhin, M., Baugh, K., Hsu, F.-C., Ghosh, T., 2016. Methods for global survey of natural gas flaring from Visible Infrared Imaging Radiometer Suite data. Energies 9(1), 14. https://doi.org/10.3390/en9010014
- Elvidge, C.D., Bazilian, M.D., Zhizhin, M., et al., 2018. The potential role of natural gas flaring in meeting greenhouse gas mitigation targets. Energy Strategy Reviews 20, 156–162. https://doi.org/10.1016/j.esr.2017.12.012
- FAO, 2015. Global Administrative Unit Layers (GAUL) 2015. Food and Agriculture Organization of the United Nations, Rome.
- Farr, T.G., Rosen, P.A., Caro, E., et al., 2007. The Shuttle Radar Topography Mission. Reviews of Geophysics 45(2), RG2004. https://doi.org/10.1029/2005RG000183
- Faruolo, M., Caseiro, A., Lacava, T., Kaiser, J.W., 2021. Gas flaring: A review focused on its analysis from space. IEEE Geoscience and Remote Sensing Magazine 9(1), 258–281. https://doi.org/10.1109/MGRS.2020.3007232
- Fawole, O.G., Cai, X.-M., MacKenzie, A.R., 2016. Gas flaring and resultant air pollution: A review focusing on black carbon. Environmental Pollution 216, 182–197. https://doi.org/10.1016/j.envpol.2016.05.075
- Fioletov, V.E., McLinden, C.A., Krotkov, N., Li, C., 2015. Lifetimes and emissions of SO_2 from point sources estimated from OMI. Geophysical Research Letters 42(6), 1969–1976. https://doi.org/10.1002/2015GL063148
- Fioletov, V.E., McLinden, C.A., Krotkov, N., et al., 2016. A global catalogue of large SO_2 sources and emissions derived from the Ozone Monitoring Instrument. Atmospheric Chemistry and Physics 16(18), 11497–11519. https://doi.org/10.5194/acp-16-11497-2016

- Fioletov, V., McLinden, C.A., Griffin, D., et al., 2020. Anthropogenic and volcanic point source SO_2 emissions derived from TROPOMI on board Sentinel-5 Precursor: First results. Atmospheric Chemistry and Physics 20(9), 5591–5607. https://doi.org/10.5194/acp-20-5591-2020
- Fisher, D., Wooster, M.J., 2019. Multi-decade global gas flaring change inventoried using the ATSR-1, ATSR-2, AATSR and SLSTR data records. Remote Sensing of Environment 232, 111298. https://doi.org/10.1016/j.rse.2019.111298
- Goldberg, D.L., Lu, Z., Streets, D.G., et al., 2019. Enhanced capabilities of TROPOMI NO_2: Estimating NO_x from North American cities and power plants. Environmental Science & Technology 53(21), 12594–12601. https://doi.org/10.1021/acs.est.9b04488
- Gorelick, N., Hancher, M., Dixon, M., Ilyushchenko, S., Thau, D., Moore, R., 2017. Google Earth Engine: Planetary-scale geospatial analysis for everyone. Remote Sensing of Environment 202, 18–27. https://doi.org/10.1016/j.rse.2017.06.031
- Gvakharia, A., Kort, E.A., Brandt, A., et al., 2017. Methane, black carbon, and ethane emissions from natural gas flares in the Bakken Shale, North Dakota. Environmental Science & Technology 51(9), 5317–5325. https://doi.org/10.1021/acs.est.6b05183
- Hansen, M.C., Potapov, P.V., Moore, R., et al., 2013. High-resolution global maps of 21st-century forest cover change. Science 342(6160), 850–853. https://doi.org/10.1126/science.1244693
- Hersbach, H., Bell, B., Berrisford, P., et al., 2020. The ERA5 global reanalysis. Quarterly Journal of the Royal Meteorological Society 146(730), 1999–2049. https://doi.org/10.1002/qj.3803
- Knippertz, P., Coe, H., Chiu, J.C., et al., 2015. The DACCIWA project: Dynamics–aerosol–chemistry–cloud interactions in West Africa. Bulletin of the American Meteorological Society 96(9), 1451–1460. https://doi.org/10.1175/BAMS-D-14-00108.1
- Landgraf, J., aan de Brugh, J., Scheepmaker, R., et al., 2016. Carbon monoxide total column retrievals from TROPOMI shortwave infrared measurements. Atmospheric Measurement Techniques 9(10), 4955–4975. https://doi.org/10.5194/amt-9-4955-2016
- Lauvaux, T., Giron, C., Mazzolini, M., et al., 2022. Global assessment of oil and gas methane ultra-emitters. Science 375(6580), 557–561. https://doi.org/10.1126/science.abj4351
- Lorente, A., Borsdorff, T., Butz, A., et al., 2021. Methane retrieved from TROPOMI: Improvement of the data product and validation of the first 2 years of measurements. Atmospheric Measurement Techniques 14(1), 665–684. https://doi.org/10.5194/amt-14-665-2021
- Mann, H.B., 1945. Nonparametric tests against trend. Econometrica 13(3), 245–259. https://doi.org/10.2307/1907187
- Ndunagu, P.N., Joel, O.F., Oji, A.A., 2021. Comparative analysis of satellite and regulatory based gas flare volumes in the Niger Delta region. Nigerian Journal of Technological Development 18(4), 279–287. https://doi.org/10.4314/njtd.v18i4.3
- NUPRC (Nigerian Upstream Petroleum Regulatory Commission), 2024. Gas Production Status Report, January to December 2021, 2023 and 2024. NUPRC, Abuja. https://www.nuprc.gov.ng/reports/gas-production-status-report (accessed 10 November 2026).
- Plant, G., Kort, E.A., Brandt, A.R., et al., 2022. Inefficient and unlit natural gas flares both emit large quantities of methane. Science 377(6614), 1566–1571. https://doi.org/10.1126/science.abq0385
- Schneising, O., Buchwitz, M., Reuter, M., et al., 2019. A scientific algorithm to simultaneously retrieve carbon monoxide and methane from TROPOMI onboard Sentinel-5 Precursor.

Atmospheric Measurement Techniques 12(12), 6771–6802. https://doi.org/10.5194/amt-12-6771-2019

- Schneising, O., Buchwitz, M., Reuter, M., et al., 2020. Remote sensing of methane leakage from natural gas and petroleum systems revisited. Atmospheric Chemistry and Physics 20(15), 9169–9182. https://doi.org/10.5194/acp-20-9169-2020
- Sen, P.K., 1968. Estimates of the regression coefficient based on Kendall's tau. Journal of the American Statistical Association 63(324), 1379–1389. https://doi.org/10.1080/01621459.1968.10480934
- Stohl, A., Klimont, Z., Eckhardt, S., et al., 2013. Black carbon in the Arctic: The underestimated role of gas flaring and residential combustion emissions. Atmospheric Chemistry and Physics 13(17), 8833–8855. https://doi.org/10.5194/acp-13-8833-2013
- Theys, N., De Smedt, I., Yu, H., et al., 2017. Sulfur dioxide retrievals from TROPOMI onboard Sentinel-5 Precursor: Algorithm theoretical basis. Atmospheric Measurement Techniques 10(1), 119–153. https://doi.org/10.5194/amt-10-119-2017
- Varon, D.J., Jacob, D.J., McKeever, J., et al., 2018. Quantifying methane point sources from fine-scale satellite observations of atmospheric methane plumes. Atmospheric Measurement Techniques 11(10), 5673–5686. https://doi.org/10.5194/amt-11-5673-2018
- Varon, D.J., McKeever, J., Jervis, D., et al., 2019. Satellite discovery of anomalously large methane point sources from oil/gas production. Geophysical Research Letters 46(22), 13507–13516. https://doi.org/10.1029/2019GL083798
- Veefkind, J.P., Aben, I., McMullan, K., et al., 2012. TROPOMI on the ESA Sentinel-5 Precursor: A GMES mission for global observations of the atmospheric composition for climate, air quality and ozone layer applications. Remote Sensing of Environment 120, 70–83. https://doi.org/10.1016/j.rse.2011.09.027
- World Bank, 2026. Global Gas Flaring Tracker Report, June 2026. Global Flaring and Methane Reduction Partnership, World Bank, Washington, DC.
- Zanaga, D., Van De Kerchove, R., Daems, D., et al., 2022. ESA WorldCover 10 m 2021 v200. Zenodo. https://doi.org/10.5281/zenodo.7254221
- Zhizhin, M., Matveev, A., Ghosh, T., et al., 2021. Measuring gas flaring in Russia with multispectral VIIRS Nightfire. Remote Sensing 13(16), 3078. https://doi.org/10.3390/rs13163078

Supplementary Files

This is a list of supplementary files associated with this preprint. Click to download.

- Supplementarycodeanddata.zip.zip